

Supersonic Plume Impingement From Second Stage Rocket Motor

Gaurav Bisht

A Dissertation Submitted to
Indian Institute of Technology Hyderabad
In Partial Fulfillment of the Requirements for
The Degree of Master of Technology

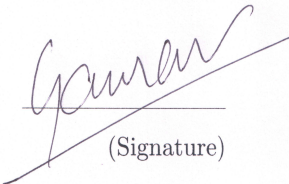


Department of Mechanical & Aerospace Engineering

June 2015

Declaration

I declare that this written submission represents my ideas in my own words, and where ideas or words of others have been included, I have adequately cited and referenced the original sources. I also declare that I have adhered to all principles of academic honesty and integrity and have not misrepresented or fabricated or falsified any idea/data/fact/source in my submission. I understand that any violation of the above will be a cause for disciplinary action by the Institute and can also evoke penal action from the sources that have thus not been properly cited, or from whom proper permission has not been taken when needed.



(Signature)

(Gaurav Bisht)

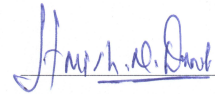
(ME13M1027)

Approval Sheet

This Thesis entitled Supersonic Plume Impingement From Second Stage Rocket Motor by Gaurav Bisht is approved for the degree of Master of Technology from IIT Hyderabad



(Dr. B. S. Subhash Chandran) Examiner
Associate Director
DRDL



(Dr. Harish N. Dixit) Examiner
Dept. of Mechanical & Aerospace Engineering
IITH



(Dr. Nishanth Dongari) Adviser
Dept. of Mechanical & Aerospace Engineering
IITH

Acknowledgements

I am grateful to my teacher who has taught me how to live a responsible life with his patience and love.

I would like to express my gratitude to my guide Dr. Nishanth Dongari to allow me the freedom to work and at the same time to keep an eye to see that I do not get drifted from the main objective. I would especially like to thank him for his moral support and calmness, at the time when I have been running on low confidence with the thesis work. His honesty and humility, has always motivated us to work harder and has kept us grounded. And simultaneously, he has been the source of motivation for all our friends. Thus, the work environment, I have got to work has been vibrant and energetic.

I would like to thank Ashwani Assam and Vatsalya Sharma for their valuable suggestion at various point of the thesis. In addition, they have helped us in understanding the *rhoCentralFoam* solver, which has been the starting point for this thesis. I would also like to thank all my friends who have always maintained an atmosphere of co-operation and friendship. Thus, have made the thesis a joyful experience.

I would like to thank my guide and the entire IIT Hyderabad system for providing us an excellent computational facility to work upon.

My thanks would also go to Dr. V. K. Saraswat, whose practical expertise in this area has boosted my interest for working in the area of high-speed flow.

At last I would like to thank my parents for their support and patience. I know, I have failed to be with them at various moments, they would have liked me to be with them.

Abstract

During the flight of a multistage rocket or missile, stage separation is one of the most critical phases. The effect of plume impingement from the upper stage nozzle on the lower stage is important in determining the separation trajectory. This plume impingement not only causes loads on the lower stage, but the later also interferes with the jet from the upper stage because the flow reversal inside the spent stage cavity is directed back toward the continuing stage. In the present study, we are investigating plume expansion and plume impingement flows from a second stage rocket nozzle. We have carried out numerical simulations with *rhoCentralFoam* solver, which is part of the open source computational fluid dynamics (CFD) software OpenFOAM (Open Field Operation and Manipulation). We have validated the compressible flow solver with the experimental results of a thrust optimized contour nozzle, for two nozzle pressure ratio (NPR) conditions : $\text{NPR} = 8$ and 20 . From computational results, detailed flow separation and shock structure are observed and are found in agreement with experimental findings. Further, *rhoCentralFoam* is utilized to carry out simulations for hot stage separation of a multistage rocket. The selected launcher is the Brazilian VLM-1 (Microsatellite Launch Vehicle-1). Our solver results are validated with the DLR tau code, for the drag and lift coefficients. Various plume deflector configurations like conical, spherical and blunt are investigated. Heat transfer, pressure and friction coefficients are reported on critical surfaces which are the top of first stage, outer surface of the second stage nozzle wall and interior of the second stage aftwall. We have investigated the effect of cone angle and separation distance between two stages for the conical configuration.

Contents

Declaration	ii
Approval Sheet	iii
Acknowledgements	iv
Abstract	v
1 Introduction	6
1.1 Literature review	7
1.2 Numerical Simulation	10
1.2.1 The rhoCentralFoam	11
1.3 Objectives of present work	11
2 Theory	12
2.1 Governing equations	12
2.2 Modelling	12
2.2.1 RANS	13
2.2.2 Turbulence models	13
2.3 Governing equations of rhoCentralFoam	14
2.4 Basic framework of rhoCentralFoam	15
2.4.1 0	15
2.4.2 system	15
2.4.3 constant	17
2.5 Numerical schemes	17
2.6 Solution and algorithm control	19
2.6.1 Linear solver control	19
2.6.2 Solution under-relaxation	21
2.6.3 PISO and SIMPLE algorithms	22
2.7 Boundaries	22
2.7.1 Specification of patch types in OpenFoam	23
2.7.2 Base types	24
2.7.3 Primitive types	25
2.7.4 Derived types	25

3	Test Cases	28
3.1	Validation of rhoCentralFoam with Fluent	28
3.2	Validation with experimental data	29
4	Results and discussion for SHEFEX-III launcher	34
4.1	Closed interstage configuration	34
4.2	open interstage configuration with nozzle flow switched off	37
4.3	open interstage configuration with nozzle flow switched on	38
4.3.1	Parametric study for various cone angle configurations	45
4.3.2	Parametric study for various separation distances with cone angle of 54°	51
5	Conclusions and future work	58
	References	59

List of Figures

2.1	structure of a rhoCentralFoam testcase.	16
2.2	patch attributes.	23
2.3	Axi-symmetric geometry using the <i>wedge</i> patch type.	24
3.1	Schematic of a supersonic delaval Nozzle. A is the inlet to the nozzle and B is the outlet of the nozzle	28
3.2	Computational domain of the simulated delaval nozzle with rhoCentralFoam and Fluent	28
3.3	Pressure contours comparison between (a)rhoCentralFoam and (b)Fluent results.	29
3.4	Mach number contours comparison between (a) rhoCentralFoam and (b) Fluent results. Both the solvers are being treated as inviscid.	29
3.5	variation of (a) pressure, (b) Mach number along the centerline of a supersonic delaval nozzle. rhoCentralFoam is validated against Fluent and both the solvers are inviscid.	30
3.6	Schematic of thrust optimized contour nozzle [1].	30
3.7	Computational domain of the supersonic nozzle flow and plume expansion-into the atmosphere. Farfield and wall boundaries are denoted and axis is symmetric.	30
3.8	Visualization of mach stem (MS), reflected shock(RS), separated shock(SS) in the supersonic nozzle flow expansion.	31
3.9	Visualization of the shock formed inside the nozzle.	32
3.10	The normalized centerline pressure variation along the axial distance for rhoCentralFoam solver against the experimental data [1]. Results are presented for nozzle pressure ratio (NPR) (a) 8 and (b) 20.	32
3.11	The normalized wall pressure variation along the axial distance for rhoCentralFoam solver against the experimental data [1]. Results are presented for nozzle pressure ratio (NPR) (a) 8 and (b) 20.	33
4.1	Computational domain for closed interstage configuration of VLM-1 (Microsatellite Launch Vehicle-1) [2].	35

4.2	variation of (a) coefficient of drag (C_d) and (b) coefficient of lift (C_l) with angle of attack. <i>rhoCentralFoam</i> solver is validated against the results of Tau code [3, 4] for closed interstage configuration.	35
4.3	Close up view of the computational domain for open interstage configuration of VLM-1 (Microsatellite Launch Vehicle-1) with the nozzle being switched off [2].	36
4.4	Variation of (a) coefficient of drag (C_d) and (b) coefficient of lift (C_l) with angle of attack. <i>rhoCentralFoam</i> solver is validated against the results of Tau code [3, 4] for open interstage configuration.	36
4.5	(a) Demonstration of the recirculation zones formed outside the nozzle and interior of aftwall for open interstage configuration. (b) Enlarged view of the recirculation zone show casing impingement shock, stagnation point and shear layer.	37
4.6	Shefex-III Launcher mesh with nozzle flow switched on and the close up view of computational domain around the nozzle.	38
4.7	Left side plots: (a), (c) and (e) show schematic computational domains of stage separation studies with blunt, conical and spherical plume deflector configurations, respectively. Right side plots: (b), (d) and (f) demonstrate velocity contours for blunt, conical and spherical configurations, respectively.	39
4.8	Left side plots show pressure contours while the right side ones demonstrate temperature contours for (a) & (b) blunt, (c) & (d) conical and (e) & (f) spherical plume deflector configurations.	40
4.9	Zoomed view of velocity contours to show case plume interaction with supersonic freestream and key recirculation zones for (a) blunt, (b) conical and (c) spherical plume deflector shapes.	41
4.10	Variation of aero-thermodynamic coefficients on the top of 1 st stage surface along the arc length and comparison between three different plume deflector shapes. Here, (a) heat transfer coefficient (C_h), (b) pressure coefficient(C_p) and (c) normalized shear stress.	42
4.11	Variation of aero-thermodynamic coefficients on the outer nozzle wall along the arc length and comparison between three different plume deflector shapes. Here, (a) heat transfer coefficient (C_h), (b) pressure coefficient (C_p) and (c) normalized shear stress.	43
4.12	Variation of aero-thermodynamic coefficients on the interior of aftwall i.e. region ‘a’ along the arc length and comparison between three different plume deflector shapes. Here, (a) heat transfer coefficient (C_h), (b) pressure coefficient (C_p) and (c) normalized shear stress.	44

4.13	(a) The density variation on the outersurface of aftwall. (b) The centerline density variation inside the nozzle starting from throat to the exit. Comparisons are made between three plume deflector shapes.	45
4.14	Zoomed view of velocity contours to demonstrate plume interaction with supersonic freestream and key recirculation zones for conical deflector with cone angles of (a) 22° , (b) 33° , (c) 54° and (d) 60°	46
4.15	Variation of aero-thermodynamic coefficients on the top of 1st stage surface along the arc length and comparison between various cone angles of 22° , 33° , 54° and (d) 60° . Here, (a) heat transfer coefficient (C_h), (b) pressure coefficient (C_p) and (c) normalized shear stress.	47
4.16	Variation of aero-thermodynamic coefficients on the outer nozzle wall along the arc length and comparison between various cone angles 22° , 33° , 54° and 60° . Here, (a) heat transfer coefficient, (b) pressure coefficient and (c) normalized shear stress.	48
4.17	Variation of aero-thermodynamic coefficients on the interior of aftwall i.e. region 'a' and comparison between various cone angles of 22° , 33° , 54° and 60° . Here, (a) heat transfer coefficient (C_h), (b) pressure coefficient (C_p) and (c) normalized shear stress.	50
4.18	(a) The density variation on the outersurface of aftwall (b) The centerline density variation inside the nozzle starting from throat to the exit. Comparisons are made between various cone angles of a conical plume deflector shape.	51
4.19	Zoomed view of velocity contours to demonstrate plume interaction with supersonic freestream and key recirculation zones for conical deflector with separation distances of (a) $(1/16)D$, (b) $(1/8)D$, (c) $(1/4)D$ and (d) $(1/2)D$ between 1st stage and second stage, where D is the nozzle diameter.	52
4.20	Variation of aero-thermodynamic coefficients on the top of 1st stage along the arc length and comparison between various separation distances. Here, (a) heat transfer coefficient (C_h), (b) pressure coefficient (C_p) and (c) normalized shear stress.	53
4.21	Variation of aero-thermodynamic coefficients on the outer nozzle wall and comparison between various separation distances. Here, (a) heat transfer coefficient (C_h), (b) pressure coefficient (C_p) and (c) normalized shear stress.	54
4.22	Variation of aero-thermodynamic coefficients on the interior of aftwall along the arc length and comparison between various separation distances. Here, (a) heat transfer coefficient (C_h), (b) pressure coefficient (C_p) and (c) normalized shear stress.	55

4.23 (a) The density variation on the outersurface of aftwall.(b) The centerline density variation inside the nozzle starting from throat to the exit. Comparisons are made between various separation distances for a conical plume deflector. 56

List of Tables

2.1	Time discretization schemes	17
2.2	Interpolation schemes	18
2.3	Interpolation schemes	18
2.4	Divergence schemes	18
2.5	Surface normal gradients for laplacian terms calculations	19
2.6	Linear solvers	19
2.7	Preconditioner options.	20
2.8	Smooth solvers.	21
2.9	Basic patch types.	24
2.10	Primitive patch field types.	26
2.11	Types derived from fixedValue.	26
2.12	Derived patch field types.	27
3.1	Chemilical equilibrium properties for a decomposed gas of Hydrogen Peroxide [1]	31
4.1	Test case conditions	34
4.2	Heat transfer coefficient on the top of 1 st stage, outer nozzle wall and region 'a' for conical, spherical and blunt configurations, respectively.	56
4.3	Heat transfer coefficient on the top of 1 st stage, outer nozzle wall and region 'a' for conical configuration with varying cone angles of 22 ⁰ , 33 ⁰ , 54 ⁰ and 60 ⁰	57
4.4	Heat transfer coefficient on the top of 1 st stage, outer nozzle wall and region 'a' for conical configuration with varying separation distance of (a) (1/16)D, (b) (1/8)D, (c) (1/4)D and (d) (1/2)D.	57

Chapter 1

Introduction

The structure of a space vehicle is affected significantly by the thermal environment induced during stage separation. Elevated temperatures reduce the strength and stiffness of the structure of vehicle. Also, the thermal gradients produce local increase in stress and distortion. Improper evaluation of these effects can result in structural failure during flight. Various flow regimes such as impingement shock, shear layers, expansion fans, flow induced noise, recirculation regions etc. are of fundamental scientific importance and directly affect the performance and endurance during flight. Taking this as the motivation, the task of simulating stage separation using *rhoCentralFoam* solver was undertaken one year ago. This solver is a part of the open source computational fluid dynamics (CFD) software OpenFOAM (Open Field Operation and Manipulation). The usage of Computational Fluid Dynamics (CFD) is widely spread today. As CPUs become more powerful and affordable, most larger companies in industry are using it today. However, investing in the required hardware and commercial licenses is still a hurdle for smaller businesses to use CFD. Open source softwares provide a cheap approach to simulations, compared to commercial software. However, the open source softwares are dependent on a more knowledgeable user than for the commercial softwares, as more freedom is provided with the software and documentation can be limited. Also, as mentioned previously, another limitation for small businesses is the need for computing power to perform simulations without having to invest in the hardware. *rhoCentralFoam* is a density based compressible flow solver based on the central-upwind scheme of kurganov and tadmor.

Compressible flows are those where dynamics (i.e pressure) is the dominant factor in density change. Generally, fluid flow is considered to be compressible if the change in density relative to the stagnation density is greater than 5%. Significant compressible effects occur at Mach number of 0.3 and greater. Compressible flow is divided often into four main flow regimes based on the local Mach number (M) of the fluid flow

- Subsonic flow regime ($M \leq 0.8$)
- Transonic flow regime ($0.8 \leq M \leq 1.2$)

- Supersonic flow regime ($M > 1$)
- Hypersonic flow regime ($M > 5$)

our focus is mainly confined to 1st stage separation which usually occurs at 16km altitude and $M > 2.5$ i.e. in the supersonic flow regime. Compressible flow may be treated as either viscous or inviscid. Viscous flows are solved by the Navier-Stokes system of equations and inviscid compressible flows are solved by Euler equations. Compressible flows have discontinuous solutions in certain cases e.g vortex sheets, contact discontinuities or shock waves. So, for compressible flows special attention is required for solution methods which will accurately capture these discontinuities. In compressible fluid flows, properties are not only transported by the flow, but also by the propagation of waves. In supersonic flow the euler equations are hyperbolic i.e.the flow is only determined by the upstream conditions. Stage separation is one of the most critical phases during the flight of a multistage launch vehicle. Understanding of the pressure forces, heat loads and flow fields during the separation aid in achieving an optimum coast time for the staging operation. The effect of plume impingement from the upper stage nozzle on the lower stage is important in determining the separation trajectory.

1.1 Literature review

The selected launcher for the stage separation simulations is VLM-1 [2] which is designed as a three-stage-rocket without fins. The 1st-stage will burn out and will be dropped at the altitude of about 16 km, for which the aerodynamic effect is still pronounced. In VLM-1 [2] hot separation technique is planned to be used, which is different from the first two SHEFEX flights that utilized the cold separation supported by a spring mechanism. The hot stage separation, which is called fire-in-the-hole (FITH) in the literature [5, 6, 7], is to drop the burn out lowest stage directly by igniting the continuing stage motor. Usually, once the lowest stage is burning out, its thrust drops rapidly but can still support control forces. Then the continuing stage is ignited and the two stages disconnect almost immediately. Thereafter the staging is driven by the continuing-stage-motor: it exhausts gases into the inter-stage volume, which can form a high pressure region ahead the top of the first stage that pushes it away, and it supplies thrust accelerating the continuing stage. To vent the exhaust gases from the continuing-stage-motor, it is planned to apply a kind of lattice inter-stage structure on VLM-1. The application of the open inter-stage adapter and the hot stage separation scheme induces serious aerodynamic problems. Therefore, an accurate predictions of aero-thermodynamic loads on critical areas is imperative for aerospace applications.

Impingement forces cause undesired motions of spacecraft, therefore additional fuel consumption for compensation. Also, impingement heat load can cause damage or destruction

of surfaces if a critical value is exceeded. In aerodynamics, similarity rules are often applied. The forces for example are expressed in dimensionless form as drag or lift coefficients dependent on dimensionless flow parameters, mainly Mach number and Reynolds number. This similarity procedure is hardly applicable to plume impingement problems. The reason is the non-uniformity of the flow, which by its nature, cannot be characterized by one Mach number and one Reynolds number. These can only be specified locally [8]. Experimental methods may lead to a safe and successful separation [9, 10, 11] but such methods are expensive and time consuming. With the advent of robust numerical technique, faster computer, CFD is playing an important role in estimating the forces and moments for separation dynamics study. Bunning et al. [12] and Liever [13] described the use of several CFD methods for stage separation aerodynamics of hyper X separation from Peegasus launch vehicle. Unsteady effects, aerodynamic database extrapolation and differences between wind tunnel and flight environments were greatly described. Mirzaei et al. [14] presented RANS calculation with RNG K-epsilon model for the separation of multi stage aerospace vehicle and studied the external flow-jet flow interaction around the body components. Paglia et al. [15] presented the CFD analysis of separation process of VEGA launch vehicle using commercial CFD solver fluent. Zhang and Zhao [16] presented the computational studies of stage separation process using unstructured chimera grid. Pamadi et al. [17] described the generation of aerodynamic data base through wind tunnel test program and CFD methods using OVERFLOW code [18]. Wang et al. [19] studied the variation of flow field and aerodynamic coefficient for various separation distances by using a series of static and dynamic viscous simulations and their numerical results for $Ma = 3.0$ was compared with the experimental data. Different plume deflectors are investigated with the CFD techniques [20]. In the present paper, the major objective is to carry out detailed stage separation studies with various plume deflector configurations and also with varying separation distance. The current study is important from the numerical simulation perspective, as we employ an open source, parallelizable CFD platform to test practical stage separation phenomenon. In the present study, the flow fields are computed by the steady Reynolds-Averaged Navier-Stokes (RANS) solver with Spalart-Allmaras one-equation turbulence model [?]. In this paper, simulations are carried out to measure temperature, pressure, velocity components, heat flux vector and shear stress tensor on critical surfaces which, are the top of first stage, outer surface of the second stage nozzle wall and interior of the second stage aftwall. Test cases cover various plume deflector configurations like conical, spherical and blunt at freestream Mach number 2.6 and at an altitude of 15.6 km. We have investigated the effect of cone angle and separation distance between two stages for the conical configuration. The various parameters which are studied include :

Coefficient of Heat : Coefficient of heat C_h along a surface is a measure of net energy flux

of the molecule impinging on the surface. It is defined as follows,

$$C_h = \frac{q_w}{\frac{1}{2}\rho_\infty U_\infty^3} \quad (1.1)$$

where, q_w is the heat flux.

Pressure coefficient : The pressure coefficient C_p shows the dynamic relative pressure over the wall. It is defined as follows,

$$C_p = \frac{p_w - p_\infty}{\frac{1}{2}\rho_\infty U_\infty^2} \quad (1.2)$$

where, the pressure p_w is pressure on the surface, p_∞ is the free-stream pressure. ρ_∞ and U_∞ is the free-stream density and velocity respectively.

Drag Coefficient : The drag Coefficient C_d along a surface is a measure of net energy flux of the molecule impinging on the surface. It is defined as follows,

$$C_d = \frac{F_d}{\frac{1}{2}\rho_\infty U_\infty^3} \quad (1.3)$$

where, F_d is the drag force per unit area, ρ_∞ and U_∞ is the free-stream density and velocity respectively. The compressible flow codes have seen development of two classes of schemes central and upwind based. The central scheme which is more suited for turbomachinery applications has been incorporated in various solvers such as *rhoCentralFoam* a solver in the OpenFOAM that incorporates a new high resolution central scheme based on the work of [21]. In this work the computational mesh is generated by the commercial software ICEM CFD [22] which is a CAD based grid generation package that supports multiblock structured, unstructured tetrahedral and unstructured hexahedral grids. Current mesh is composed of unstructured tetrahedral mesh.

Nomenclature

C_h	heat transfer coefficient
C_p	pressure coefficient
C_D	drag coefficient
p	pressure
T	temperature
U	velocity
U_x	axial velocity
U_y	radial velocity
c_p	specific heat at constant pressure
H	specific enthalpy
k	thermal conductivity
R	gas constant
B	Reynolds number
Pr	Prandtl number
Kn	Knudsen number
Ma	Mach number
<i>Greek letters</i>	
ρ	density
λ	mean free path
μ	dynamic viscosity
σ_v	tangential momentum accommodation coefficient
σ_T	thermal accommodation coefficient
γ	ratio of specific heats
<i>Subscript</i>	
∞	freestream condition
f	fluid
w	wall
x	axial co-ordinate
y	normal co-ordinate
0	stagnation condition

1.2 Numerical Simulation

OpenFOAM is produced by OpenCFD Ltd. It contains over 80 solver applications to simulate specific problems in engineering. It has been released as open source since 2004. OpenFoam uses C++ as its base language as it provides the advantage of object-oriented programming language. It incorporates many class libraries for efficient development of CFD

codes. Implementation of tensor fields, partial differential equations, boundary conditions and so on, can be handled using these libraries [23]. It has become a popular tool in the scientific and OpenSource community [24, 25].

1.2.1 The rhoCentralFoam

The rhoCentralFoam is the Density-based compressible flow solver based on central-upwind schemes of Kurganov and Tadmor [26, 27]. Christopher et al [28] gives the detail of this solver and validation against standard test cases. Various compressible solver has been compared in literature and shown to be better for high speed flows [29, 30].

CFL critiria

RhocalFoam is an explicit solver,so we have time stepping criteria.The Courant-Friedrich-Lewy condition is a numerical constraint which determines the allowed time step for a specific grid size. This constraint determines that information can only propagate no further than one cell away from the original cell. In explicit schemes this constraint is necessary for convergence. If information propagates with the speed u ,then the CFL number is given in equation for a one dimensional case.

$$u \frac{\Delta t}{\Delta x} < C$$

where, C is a number which determines the CFL condition. For explicit schemes $C < 1$ is required, but it can be larger for implicit schemes.

1.3 Objectives of present work

- To validate the solver with fluent.
- To validate the solver with experimental data of of thrust optimized contour nozzle [1].
- To validate the solver with DLR tau code [3, 4] with open and closed interstage.
- To study the effect of various plume deflector configuration on the top of 1st stage.
- To do the parametric study with varying cone angles of 1st stage.
- To do the parametric study with varying distances between 1st stage and 2nd stage.

Chapter 2

Theory

2.1 Governing equations

The governing equation of fluids consists of:

continuity equation:

$$\frac{\partial \rho}{\partial t} + \frac{\partial(u_i \rho)}{\partial x_i} = 0$$

momentum equation:

$$\left(\frac{\partial \rho u_i}{\partial t} + \frac{\partial \rho u_i u_j}{\partial x_j} \right) = -\frac{\partial p}{\partial x_i} + \frac{\partial}{\partial x_j} \left(\mu \left(\frac{\partial u_i}{\partial x_j} + \frac{\partial u_j}{\partial x_i} \right) - \frac{2}{3} \mu \left(\frac{\partial u_k}{\partial x_k} \right) \delta_{ij} \right) + \rho f_i$$

Energy balance equation:

$$\left(\frac{\partial \rho E}{\partial t} + \frac{\partial \rho u_j E}{\partial x_j} \right) = -\frac{\partial p u_j}{\partial x_j} + \frac{\partial u_i \tau_{ji}}{\partial x_j} + \frac{\partial}{\partial x_j} \left(K \frac{\partial T}{\partial x_j} \right) + S_E$$

where f_i is a force applied on the fluid, S_E is the energy source term and the tensor

$$\tau_{ij} = \mu \left(\frac{\partial u_i}{\partial x_j} + \frac{\partial u_j}{\partial x_i} \right) - \frac{2}{3} \mu \left(\frac{\partial u_k}{\partial x_k} \right)$$

Equations of state relate pressure $p=p(\rho,T)$ and internal energy $i=i(\rho,T)$ to the variables ρ and T . An example of this relation is the equations of state for an ideal gas

$$p = \rho * R * T$$

2.2 Modelling

To solve the governing equations some simplifications have to be made. To remove dependence on small fluctuations usually the Reynolds Averaged Navier-Stokes assumption is used. There are other models, more advanced (and computationally heavy) as LES and DNS, but they will not be covered in this thesis.

2.2.1 RANS

To model the Reynolds Averaged Navier Stokes equation, all variables are split into a time-averaged part and a fluctuating part, $\phi = \bar{\phi} + \phi'$. The time averaged part is calculated as $\bar{\phi} = \frac{1}{T} \int_T \phi(x, t) dt$. For compressible flows often another form of decomposition is done using Favre-averaging. Here variables are decomposed as $\theta = \tilde{\theta} + \theta''$, where $\theta'' = \bar{\rho}\theta/\bar{\rho}$. Thus θ'' not only includes the turbulent fluctuations but also the density fluctuations. After Favre averaging the velocity and energy and performing a standard time-averaging for ρ and p , the following equations are derived.

$$\frac{\partial \bar{\rho}}{\partial t} + \frac{\partial(\bar{\rho}\tilde{u}_i)}{\partial x_i} = 0$$

$$\left(\frac{\partial \bar{\rho}\tilde{u}_i}{\partial t} + \frac{\partial \bar{\rho}\tilde{u}_j\tilde{u}_i}{\partial x_j}\right) = -\frac{\partial \bar{p}}{\partial x_i} + \frac{\partial}{\partial x_j}(\bar{\tau}_{ij} - \rho u_i'' u_j'')$$

Here, $\tau_{ij} = \frac{\partial}{\partial x_j}(\mu(\frac{\partial u_i}{\partial x_j} + \frac{\partial u_j}{\partial x_i}) - \frac{2}{3}\mu(\frac{\partial u_k}{\partial x_k})\delta_{ij})$ and $\bar{\tau}_{ij} = \bar{\tau}_{ij} + \tau_{ij}''$. For the energy equation a similar transformation is done with the resulting Favre averaged equation,

$$\left(\frac{\partial \bar{\rho}\tilde{E}}{\partial t} + \frac{\partial \bar{\rho}\tilde{E}\tilde{u}_j}{\partial x_j}\right) = -\frac{\partial \bar{p}\tilde{u}_j}{\partial x_j} + \frac{\partial \tilde{u}_i \bar{\tau}_{ji}}{\partial x_j} - \frac{\partial}{\partial x_j}(\bar{q}_j) - \frac{\partial}{\partial x_j}(u_j' p)$$

2.2.2 Turbulence models

When modeling the governing equations with RANS, the need to model the turbulent scales is apparent. There are several models which deal with how to model turbulence. Here only the Spalart-Allmaras model will be reviewed.

Spalart-Allmaras

The turbulence model Spalart-Allmaras is an one equation model, where the kinematic eddy viscosity is calculated through a transport equation and a length scale is found from an algebraic expression. The model is a cheap way of calculating the boundary layers in aerodynamics. In the Spalart-Allmaras model an eddy viscosity parameter $\tilde{\nu}$ is calculated. It is related to eddy viscosity as:

$$\nu_t = \tilde{\nu} f_{v_1}$$

The Reynolds stresses are calculated using the following assumption,

$$-\bar{\rho} u_i' u_j' = \rho \tilde{\nu} f_{v_1} \left(\frac{\partial \bar{u}_i}{\partial x_j} + \frac{\partial \bar{u}_j}{\partial x_i} \right)$$

A transport equation is set up for $\tilde{\nu}$ to find the eddy viscosity,

$$\left(\frac{\partial \rho \tilde{\nu}}{\partial t} + \frac{\partial \rho \tilde{\nu} \bar{u}_k}{\partial x_k}\right) = \frac{1}{\sigma_v} \left[\frac{\partial}{\partial x_k} ((\mu + \rho \tilde{\nu}) \frac{\partial \tilde{\nu}}{\partial x_k}) + C_{b_2} \rho \frac{\partial \tilde{\nu}}{\partial x_k} \frac{\partial \tilde{\nu}}{\partial x_k} \right] + C_{b_1} \rho \tilde{\nu} \tilde{\Omega} - C_{w_1} \rho \left(\frac{\tilde{\nu}}{\kappa y} \right)^2 f_w$$

Where $\tilde{\Omega} = \Omega + \frac{\tilde{\nu}}{(\kappa y)^2} f_{v_2}$, and Ω is the mean vorticity. The wall functions are dependent on the following functions $f_{v_2} = f_{v_2}(\frac{\tilde{\nu}}{\nu})$ and $f_w = f_w(\frac{\tilde{\nu}}{(\Omega \kappa^2 y^2)})$. The turbulent length scale can be found from κy , where y is the distance from the wall. The model constants are set as $\sigma_v = 2/3$, $\kappa = 0.4187$, $C_{b_1} = 0.1355$, $C_{b_2} = 0.622$ and $C_{w_1} = 0.56203$ [31]

2.3 Governing equations of rhoCentralFoam

This solver is solving each of the governing compressible equations separately. First the continuity equation is solved, providing a new value for ρ .

$$\frac{\partial \rho}{\partial t} + \frac{\partial(u_i \rho)}{\partial x_i} = 0$$

The continuity equation, is solved with the previous time step velocity values. For convention purposes

$$\hat{u}_i = \rho u_i$$

and

$$\hat{E} = \rho E$$

$$\left(\frac{\partial \hat{u}_i}{\partial t}\right)_I + \frac{\partial(u_i \hat{u}_j)}{\partial x_j} + \frac{\partial \rho}{\partial x_i} = 0$$

It explicitly calculates \hat{u}_i . thus no linear solver is required.

The time derivative $\left(\frac{\partial}{\partial t}\right)_I$ is only the inviscid contributions. The new velocity u_i is updated by using the updated density ρ .

thus

$$u_i = \frac{\hat{u}_i}{\rho}$$

The diffusion correction equation is now solved for u_i where the viscous terms are added.

$$\left(\frac{\partial(\rho u_i)}{\partial t}\right)_V - \frac{\partial}{\partial x_j} \left(\mu \frac{\partial u_i}{\partial x_j}\right) - \frac{\partial}{\partial x_j} \mu \left(\frac{\partial u_j^{exp}}{\partial x_i} - \frac{2}{3} \left(\frac{\partial u_k^{exp}}{\partial x_k}\right) \delta_{ij}\right) = 0$$

In the equation the time derivative $\left(\frac{\partial}{\partial t}\right)_V$ is the contribution of diffusion and viscous forces. The velocities u_j^{exp} are taken from the solution of the inviscid equation. The laplacian term is added implicitly in u_i and solved for with a linear solver available in OpenFOAM. A similar procedure is done for the energy equation. First \hat{E} at the new time step is found explicitly from the equation. found explicitly from the equation,

$$\left(\frac{\partial \hat{E}}{\partial t}\right)_I + \frac{\partial}{\partial x_k} [u_k (\hat{E} + p)] - \frac{\partial}{\partial x_i} \mu (u_j) \left[\frac{\partial u_j^{exp}}{\partial x_i} + \frac{\partial u_i^{exp}}{\partial x_j} - \frac{2}{3} \left(\frac{\partial u_k^{exp}}{\partial x_k}\right) \delta_{ij}\right] = 0$$

From \hat{E} the Temperature T is calculated through

$$T = \frac{1}{c_v} \left(\frac{\hat{E}}{\rho} - \frac{u_k u_k}{2} \right)$$

Then a diffusion correction equation for T is solved to include the diffusive terms,

$$\left(\frac{\partial(\rho c_v T)}{\partial t} \right)_V - \frac{\partial}{\partial x_k} \left(k \frac{\partial T}{\partial x_k} \right) = 0$$

The diffusion correction equation for T is carried out implicitly, thus the laplacian of T is taken at the new time step. An iterative solver of choice is used to solve this system of equations. After the temperature is calculated the temperature dependent quantities k and μ are evaluated at the new temperature T. Also the pressure,

$$p = \rho * R * T$$

is updated. The variables k, μ and p are held constant through each iteration and only updated at the end of it.

2.4 Basic framework of rhoCentralFoam

In *rhoCentralFoam* a certain structure of the input files is expected. A case has to be set up in a predestined manner which contains a minimum of three directories. A *constant* folder and a *system* folder are needed. Also a time folder is needed, this is usually named 0, but can be named differently if 0 is not the starting time. There are also subfolders and files that are contained in the mentioned folders, a few options are reviewed here. The structure of a rhoCentralFoam case can be seen in figure 2.1.

2.4.1 0

This folder contains files with the initial conditions of the used variables. For laminar compressible Navier-Stokes equation only files containing the initial conditions of U, T and p are needed. For turbulence models other variables will need to be added as well. Three entries have to be done for each variable file. The dimension of the variable is assigned through dimensions in the file (for instance m/s for the velocity). The internal field is assigned through *internalField* and the boundary field is given through *boundaryField* [32].

2.4.2 system

This folder contains the specifications for the simulation. In the *decomposeParDict* file the mesh is decomposed into an assigned number of parts for parallel simulations. The

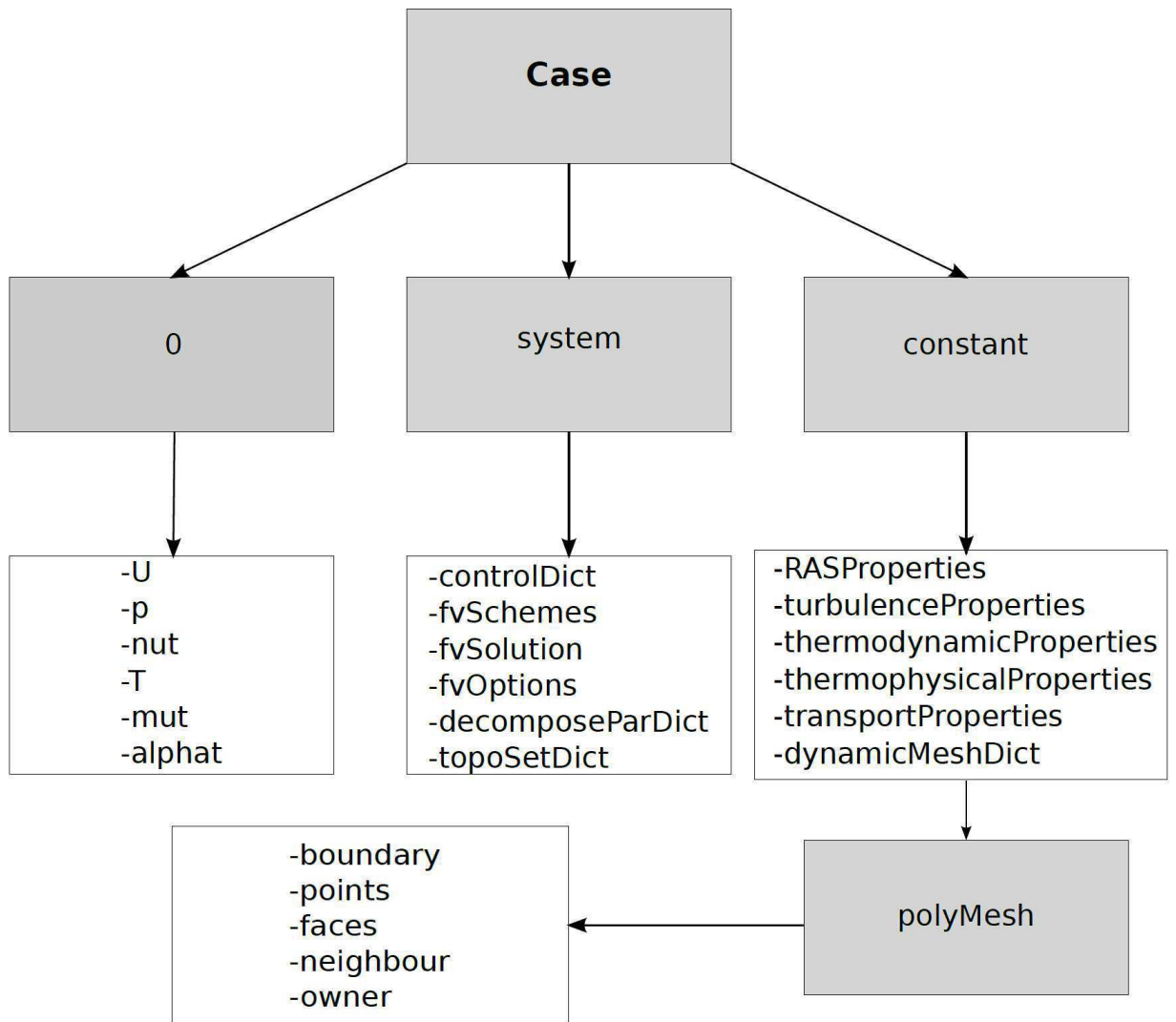


Figure 2.1: structure of a rhoCentralFoam testcase.

topoSetDict creates sets in the mesh, which can be used to define areas with extra source terms. In *controlDict* the frequency of solution file outputs, run time, time steps and Courant number are assigned [32].

2.4.3 constant

This folder contains specifications for turbulence and fluid properties. Depending on the solver chosen, different files need to be specified. For all solvers which calculate the RANS equations, the file *RASProperties* determines the turbulence model used. The type of turbulence model applied is determined in *turbulenceProperties* where either LES, RAS or laminar model can be chosen. For incompressible solvers the file *transportProperties* determines the behavior of the kinematic viscosity ν . For the compressible solver *rhoCentralFoam* temperature dependency is determined in the files *thermodynamicProperties* and *thermophysicalProperties*.

polymesh

rhoCentralFoam uses a cell-centered control volume for its calculations. In the *polyMesh* folder files are contained describing the mesh. These files include *points*, which contain the points of the mesh. *faces*, which contain the faces of the cells. *owner*, that contains what faces belong to a cell and neighbour which contains the information about the connectivity between cells. Also the boundaries are given in the file *boundary*, here the boundaries are assigned names and also of what type they are, such as empty, wall or patch for instance [32].

2.5 Numerical schemes

The *fvSchemes* dictionary in the *system* directory sets the numerical schemes for terms, such as derivatives in equations, that appear in applications being run. In the *fvSchemes* file the numerical discretization schemes for the different components in the modeled equations are assigned. For time discretization the schemes shown in table 2.1 are available. They are assigned under *ddtSchemes* in the *fvSchemes* file. In the CrankNicholson case a blending function parameter $\varphi \in [0,1]$ can be chosen.

Euler	First order, bounded, implicit
localEuler	Local-time step, first order, bounded, implicit
CrankNicholson φ	Second order, bounded, implicit
backward	Second order, implicit
steadyState	No solving of time derivatives

Table 2.1: Time discretization schemes

For $\varphi = 1$, the normal Crank-Nicholson scheme is used, whereas if $\varphi = 0$ is chosen it corresponds to an Euler scheme [32]. Available interpolation schemes are given in table 2.2.

These are assigned under *interpolationSchemes*.

linear	Linear interpolation
cubicCorrection	Cubic scheme
midPoint	Linear interpolation with symmetric weighting

Table 2.2: Interpolation schemes

There are also upwind schemes that can be used for interpolation, but these are seldom used except for convective terms. Gradients can be discretized as seen in table 2.3 and are assigned under *gradSchemes*. Interpolation schemes used for gradient calculations, are generally chosen to be a centered scheme such as linear or cubic interpolation. Upwind based interpolation is available but seldom used for this purpose.

Gauss <interpolationScheme>	Second order, Gaussian integration
leastSquares	Second order, least squares
fourth	Fourth order, least squares
cellLimited <gradScheme>	Cell limited version of one of the above schemes
faceLimited <gradScheme>	Face limited version of one of the above schemes

Table 2.3: Interpolation schemes

For discretization of divergence terms the schemes are presented in table 2.4 and assigned under *divSchemes*. Other interpolation schemes than upwind based schemes can be used. For instance the centered schemes of table 2.2 are available for discretization, but seldom used.

upwind	First order bounded
linearUpwind	First/second order linear upwind scheme, bounded
QUICK	First/second order bounded
TVD schemes	First/second order bounded
SFCD	Second order bounded
NVD schemes	First/Second order bounded

Table 2.4: Divergence schemes

For laplacian terms an interpolation scheme is required for interpolation of diffusion coefficients and also a surface normal gradient scheme for the surface gradient. As the possible interpolation schemes already have been mentioned in table 2.2. Only the surface normal schemes are presented in table 2.5. The laplacian terms are assigned under *laplacianSchemes*. The limited correction has to be assigned a value to $\phi \in [0,1]$, which determines how much non-orthogonal correction is made.

corrected	Explicit non-orthogonal correction
uncorrected	No non-orthogonal correction
bounded	Bounded correction
limited ϕ	Limited non-orthogonal correction
fourth	Fourth order

Table 2.5: Surface normal gradients for laplacian terms calculations

2.6 Solution and algorithm control

The equation solvers, tolerances and algorithms are controlled from the *fvSolution* dictionary in the *system* directory. *fvSolution* contains a set of subdictionaries that are specific to the solver being run. However, there is a small set of standard subdictionaries that cover most of those used by the standard solvers. These subdictionaries include *solvers*, *relaxationFactors*, *PISO* and *SIMPLE*.

2.6.1 Linear solver control

The first sub-dictionary that appears in all solver applications, is *solvers*. It specifies each linear-solver that is used for each discretised equation; it is emphasised that the term linear-solver refers to the method of number-crunching to solve the set of linear equations, as opposed to *application* solver which describes the set of equations and algorithms to solve a particular problem. The term linear-solver is abbreviated to solver. The syntax for each entry within *solvers* uses a keyword that is the word relating to the variable being solved in the particular equation. The solver is selected through the *solver* keyword from the choices available in OpenFOAM.

Solver	Keyword
Preconditioned (bi-)conjugate gradient	PCG/PBiCG
Solver using a smoother	smoothSolver
Generalised geometric-algebraic multi-grid	GAMG
Diagonal solver for explicit systems	diagonal

Table 2.6: Linear solvers

PCG is for symmetric matrices, PBiCG is for asymmetric matrices. The solvers distinguish between symmetric matrices and asymmetric matrices. The symmetry of the matrix depends on the structure of the equation being solved and, while the user may be able to determine this, it is not essential since OpenFOAM will produce an error message to advise the user if an inappropriate solver has been selected.

Solution tolerances

The sparse matrix solvers are iterative, i.e. they are based on reducing the equation residual over a succession of solutions. The residual is ostensibly a measure of the error in the

solution so that the smaller it is, the more accurate the solution. More precisely, the residual is evaluated by substituting the current solution into the equation and taking the magnitude of the difference between the left and right hand sides; it is also normalised to make it independent of the scale of the problem being analysed. Before solving an equation for a particular field, the initial residual is evaluated based on the current values of the field. After each solver iteration the residual is re-evaluated. The solver stops if either of the following conditions are reached:

- the residual falls below the *solver tolerance*, `tolerance`;
- the ratio of current to initial residuals falls below the *solver relative tolerance*, `relTol`;
- the number of iterations exceeds a *maximum number of iterations*, `maxIter`;

The solver tolerance should represent the level at which the residual is small enough that the solution can be deemed sufficiently accurate. The solver relative tolerance limits the relative improvement from initial to final solution. In transient simulations, it is usual to set the solver relative tolerance to 0 to force the solution to converge to the solver tolerance in each time step. The tolerances, `tolerance` and `relTol` must be specified in the dictionaries for all solvers; `maxIter` is optional.

Preconditioned conjugate gradient solvers

There are a range of options for preconditioning of matrices in the conjugate gradient solvers, represented by the `preconditioner` keyword in the solver dictionary. The preconditioners are listed in Table 2.7.

Preconditioner	Keyword
Diagonal incomplete-Cholesky (symmetric)	DIC
Faster diagonal incomplete-Cholesky (DIC with caching)	FDIC
Diagonal incomplete-LU (asymmetric)	DILU
Diagonal	diagonal
Geometric-algebraic multi-grid	GAMG
No preconditioning	none

Table 2.7: Preconditioner options.

Smooth solvers

The solvers that use a smoother require the smoother to be specified. The smoother options are listed in Table 2.8. Generally `GaussSeidel` is the most reliable option, but for bad matrices DIC can offer better convergence. In some cases, additional post-smoothing using `GaussSeidel` is further beneficial, i.e. the method denoted as `DICGaussSeidel`. The user must also specify the number of sweeps, by the `nSweeps` keyword, before the residual is recalculated, following the tolerance parameters.

smoother	Keyword
Gauss-Seidel	GaussSeidel
Diagonal incomplete-Cholesky (symmetric)	DIC
Diagonal incomplete-Cholesky with Gauss-Seidel (symmetric)	DICGaussSeidel

Table 2.8: Smooth solvers.

Geometric-algebraic multi-grid solvers

The generalised method of geometric-algebraic multi-grid (GAMG) uses the principle of: generating a quick solution on a mesh with a small number of cells; mapping this solution onto a finer mesh; using it as an initial guess to obtain an accurate solution on the fine mesh. GAMG is faster than standard methods when the increase in speed by solving first on coarser meshes outweighs the additional costs of mesh refinement and mapping of field data. In practice, GAMG starts with the mesh specified by the user and coarsens/refines the mesh in stages. The user is only required to specify an approximate mesh size at the most coarse level in terms of the number of cells `nCoarsestCells`.

The agglomeration of cells is performed by the algorithm specified by the `agglomerator` keyword. Presently we recommend the `faceAreaPair` method. It is worth noting there is an `MGridGen` option that requires an additional entry specifying the shared object library for `MGridGen`.

In the experience of OpenCFD, the `MGridGen` method offers no obvious benefit over the `faceAreaPair` method. For all methods, agglomeration can be optionally cached by the `cacheAgglomeration` switch.

Smoothing is specified by the `smoother` which are specified in table 2.8. The number of sweeps used by the smoother at different levels of mesh density are specified by the `nPreSweeps`, `nPostSweeps` and `nFinestSweeps` keywords. The `nPreSweeps` entry is used as the algorithm is coarsening the mesh, `nPostSweeps` is used as the algorithm is refining, and `nFinestSweeps` is used when the solution is at its finest level.

The `mergeLevels` keyword controls the speed at which coarsening or refinement levels is performed. It is often best to do so only at one level at a time, i.e. `set mergeLevels 1`. In some cases, particularly for simple meshes, the solution can be safely speeded up by coarsening/refining two levels at a time, i.e. setting `mergeLevels 2`.

2.6.2 Solution under-relaxation

A second sub-dictionary of `fvSolution` that is often used in OpenFOAM is `relaxationFactors` which controls under-relaxation, a technique used for improving stability of a computation, particularly in solving steady-state problems. Under-relaxation works by limiting the amount which a variable changes from one iteration to the next, either by modifying the solution matrix and source prior to solving for a field or by modifying the field directly. An under-relaxation factor α , $0 < \alpha \leq 1$ specifies the amount of under-relaxation, as described

below.

- No specified α : no under-relaxation. .
- $\alpha = 1$: guaranteed matrix diagonal equality/dominance.
- α decreases, under-relaxation increases.
- $\alpha = 0$: solution does not change with successive iterations.

An optimum choice of α is one that is small enough to ensure stable computation but large enough to move the iterative process forward quickly; values of α as high as 0.9 can ensure stability in some cases and anything much below, say, 0.2 are prohibitively restrictive in slowing the iterative process.

2.6.3 PISO and SIMPLE algorithms

Most fluid dynamics solver applications in OpenFOAM use the pressure-implicit split-operator (PISO) or semi-implicit method for pressure-linked equations (SIMPLE) algorithms. These algorithms are iterative procedures for solving equations for velocity and pressure, PISO being used for transient problems and SIMPLE for steady-state.

Both algorithms are based on evaluating some initial solutions and then correcting them. SIMPLE only makes 1 correction whereas PISO requires more than 1, but typically not more than 4. The user must therefore specify the number of correctors in the PISO dictionary by the `nCorrectors` keyword .

An additional correction to account for mesh non-orthogonality is available in both SIMPLE and PISO in the standard OpenFOAM solver applications. A mesh is orthogonal if, for each face within it, the face normal is parallel to the vector between the centres of the cells that the face connects, e.g. a mesh of hexahedral cells whose faces are aligned with a Cartesian coordinate system. The number of non-orthogonal correctors is specified by the `nNonOrthogonalCorrectors` keyword . The number of non-orthogonal correctors should correspond to the mesh for the case being solved, i.e. 0 for an orthogonal mesh and increasing with the degree of non-orthogonality up to, say, 20 for the most non-orthogonal meshes.

2.7 Boundaries

In this section we discuss the way in which boundaries are treated in OpenFOAM. The subject of boundaries is a little involved because their role in modelling is not simply that of a geometric entity but an integral part of the solution and numerics through boundary conditions or inter-boundary connections.

We first need to consider that, for the purpose of applying boundary conditions, a boundary is generally broken up into a set of patches. One patch may include one or

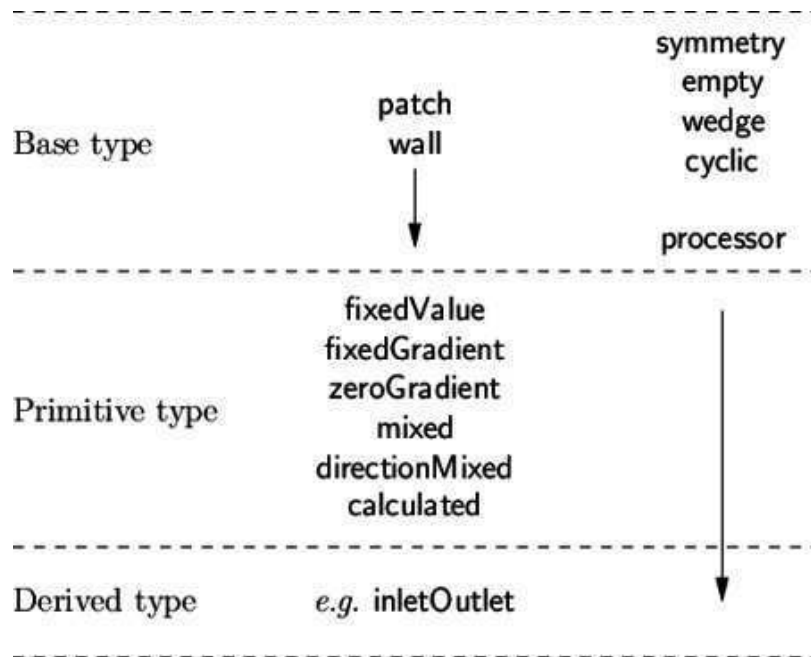


Figure 2.2: patch attributes.

more enclosed areas of the boundary surface which do not necessarily need to be physically connected. There are three attributes associated with a patch. They are:

There are three attributes associated with a patch. They are:

Base type

The type of patch described purely in terms of geometry or a data communication link.

Primitive type

The base numerical patch condition assigned to a field variable on the patch.

Derived type

A complex patch condition, derived from the primitive type, assigned to a field variable on the patch.

2.7.1 Specification of patch types in OpenFOam

The patch types are specified in the mesh and field files of a OpenFOAM case. More precisely:

- the base type is specified under the `type` keyword for each patch in the *boundary* file, located in the *constant/polyMesh* directory;

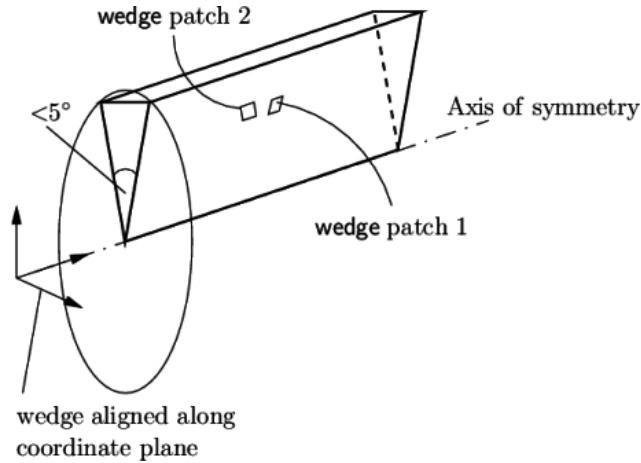


Figure 2.3: Axi-symmetric geometry using the *wedge* patch type.

- the numerical patch type, be it a primitive or derived type, is specified under the **type** keyword for each patch in a field file.

2.7.2 Base types

The base and geometric types are described below; the keywords used for specifying these types in OpenFOAM are summarised in Table 2.9.

Selection Key	Description
<code>patch</code>	generic patch
<code>symmetryPlane</code>	plane of symmetry
<code>empty</code>	front and back planes of a 2D geometry
<code>wedge</code>	wedge front and back for an axi-symmetric geometry
<code>cyclic</code>	cyclic plane
<code>wall</code>	wall used for wall functions in turbulent flows
<code>processor</code>	inter-processor boundary

Table 2.9: Basic patch types.

patch

The basic patch type for a patch condition that contains no geometric or topological information about the mesh (with the exception of *wall*), e.g. an inlet or an outlet.

wall

There are instances where a patch that coincides with a wall needs to be identifiable as such, particularly where specialist modelling is applied at wall boundaries. A good example

is wall turbulence modelling where a wall must be specified with a *wall* patch type, so that the distance from the wall to the cell centres next to the wall are stored as part of the patch.

symmetryPlane

For a symmetry plane.

empty

While OpenFOAM always generates geometries in 3 dimensions, it can be instructed to solve in 2 (or 1) dimensions by specifying a special *empty* condition on each patch whose plane is normal to the 3rd (and 2nd) dimension for which no solution is required.

wedge

For 2 dimensional axi-symmetric cases, e.g. a cylinder, the geometry is specified as a wedge of small angle (e.g. $\pi/5$) and 1 cell thick running along the plane of symmetry, straddling one of the coordinate planes, as shown in Figure 2.3. The axi-symmetric wedge planes must be specified as separate patches of *wedge* type.

cyclic

Enables two patches to be treated as if they are physically connected; used for repeated geometries, e.g. heat exchanger tube bundles. One cyclic patch is linked to another through a *neighbourPatch* keyword in the *boundary* file. Each pair of connecting faces must have similar area to within a tolerance given by the *matchTolerance* keyword in the *boundary* file. Faces do not need to be of the same orientation.

processor

If a code is being run in parallel, on a number of processors, then the mesh must be divided up so that each processor computes on roughly the same number of cells. The boundaries between the different parts of the mesh are called *processor* boundaries.

2.7.3 Primitive types

The primitive types are listed in Table 2.10.

2.7.4 Derived types

There are numerous derived types of boundary conditions in OpenFOAM, too many to list here. Instead a small selection is listed in Table 2.11,2.12.

Type	Description of condition for patch field ϕ	Data to specify
<i>fixedValue</i>	Value of ϕ is specified	value
<i>fixedGradient</i>	Normal gradient of ϕ is specified	gradient
<i>zeroGradient</i>	Normal gradient of ϕ is zero	-
<i>calculated</i>	Boundary field ϕ derived from other fields	-
<i>mixed</i>	Mixed <i>fixedValue</i> / <i>fixedGradient</i> condition depending on the value in <i>valueFraction</i>	refValue, refGradient, valueFraction, value
<i>directionMixed</i>	A mixed condition with tensorial <i>valueFraction</i> , e.g. for different levels of mixing in normal and tangential directions	refValue, refGradient, valueFraction, value

Table 2.10: Primitive patch field types.

Types derived from <i>fixedValue</i>		Data to specify
<i>movingWallVelocity</i>	Replaces the normal of the patch value so the flux across the patch is zero	value
<i>pressureInletVelocity</i>	When \mathbf{p} is known at inlet, \mathbf{U} is evaluated from the flux, normal to the patch	value
<i>pressureDirectedInletVelocity</i>	When \mathbf{p} is known at inlet, \mathbf{U} is evaluated from the flux in the inletDirection	value, inletDirection
<i>surfaceNormalFixedValue</i>	Specifies a vector boundary condition, normal to the patch, by its magnitude; +ve for vectors pointing out of the domain	value
<i>totalPressure</i>	Total pressure $p_0 = p + \frac{1}{2}\rho U ^2$ is fixed; when \mathbf{U} changes, \mathbf{p} is adjusted accordingly	p_0
<i>turbulentInlet</i>	Calculates a fluctuating variable based on a scale of a mean value	referenceField, fluctuationScale

Table 2.11: Types derived from *fixedValue*.

Types derived from <i>fixedGradient/zeroGradient</i>		Data to specify
<i>fluxCorrectedVelocity</i>	Calculates normal component of \mathbf{U} at inlet from flux	value
<i>buoyantPressure</i>	Sets <i>fixedGradient</i> pressure based on the atmospheric pressure gradient	-
Types derived from mixed		
<i>inletOutlet</i>	Switches \mathbf{U} and \mathbf{p} between <i>fixedValue</i> and <i>zeroGradient</i> depending on direction of \mathbf{U}	inletValue,value
<i>outletInlet</i>	Switches \mathbf{U} and \mathbf{p} between <i>fixedValue</i> and <i>zeroGradient</i> depending on direction of \mathbf{U}	outletValue,value
<i>pressureInletOutletVelocity</i>	Combination of <i>pressureInletVelocity</i> and <i>inletOutlet</i>	value
<i>pressureDirectedInletOutletVelocity</i>	Combination of <i>pressureDirectedInletVelocity</i> and <i>inletOutlet</i>	value,inletDirection
<i>pressureTransmissive</i>	Transmits supersonic pressure waves to surrounding pressure p_∞	pInf
<i>supersonicFreeStream</i>	Transmits oblique shocks to surroundings at $p_\infty, T_\infty, U_\infty$	pInf, TInf, UInf
Other types		
<i>slip</i>	<i>zeroGradient</i> if ϕ is a scalar; if ϕ is a vector, normal component is <i>fixedValue</i> zero, tangential components are <i>zeroGradient</i>	-
<i>partialSlip</i>	Mixed <i>zeroGradient/ slip</i> condition depending on the <code>valueFraction</code> ; = 0 for slip	valueFraction

Table 2.12: Derived patch field types.

Chapter 3

Test Cases

3.1 Validation of rhoCentralFoam with Fluent

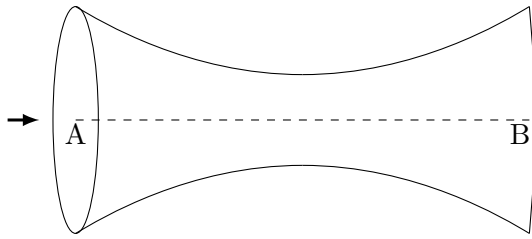


Figure 3.1: Schematic of a supersonic deLaval Nozzle. A is the inlet to the nozzle and B is the outlet of the nozzle

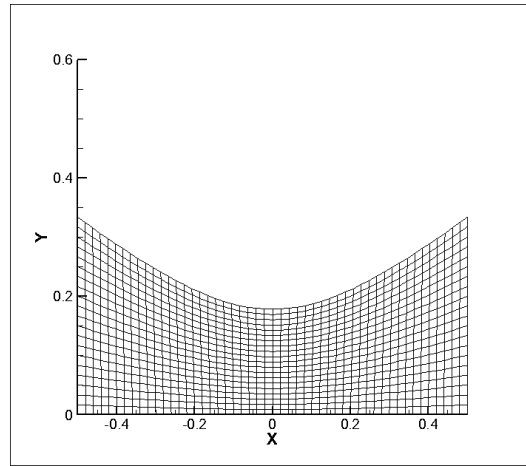


Figure 3.2: Computational domain of the simulated deLaval nozzle with rhoCentralFoam and Fluent

Here, we are validating the *rhoCentralFoam* with a commercial software Fluent, for supersonic flow case. Figs 3.1 and 3.2 show the schematic and the computational mesh for a supersonic deLaval nozzle. Consider air flowing at high-speed through a convergent-divergent nozzle having a circular cross-sectional area, A , that varies with axial distance x , according to the formula

$$A = 0.1 + x^2; -0.5 < x < 0.5. \quad (3.1)$$

where A is in square meters and x is in meters. Here $x = 0$ located at throat, $x = -0.5$ at the inlet and $x = 0.5$ at the exit. The stagnation pressure P_0 at the inlet is 101,325 Pa, the stagnation temperature T_0 at the inlet is 300 K and the static pressure p at the exit is 3,738.9 Pa. The Reynolds number for this high-speed flow is very large ($> 10^5$). Hence,

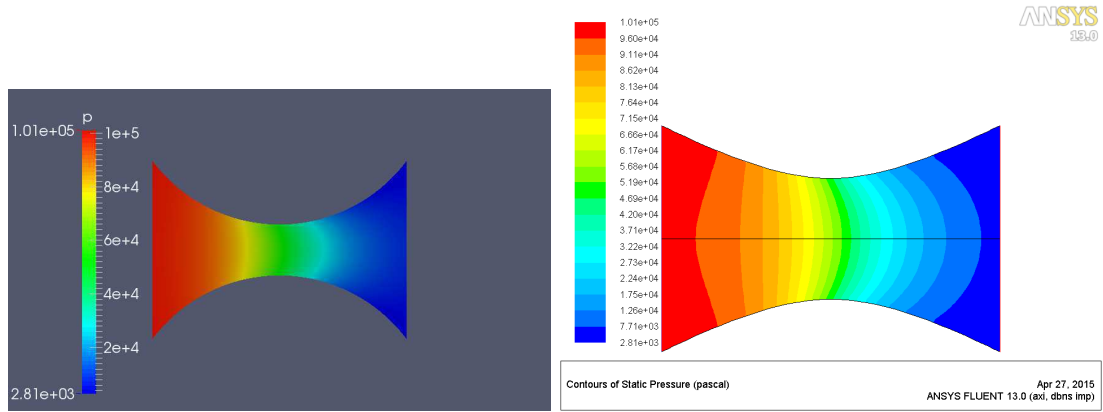


Figure 3.3: Pressure contours comparison between (a)rhoCentralFoam and (b)Fluent results.

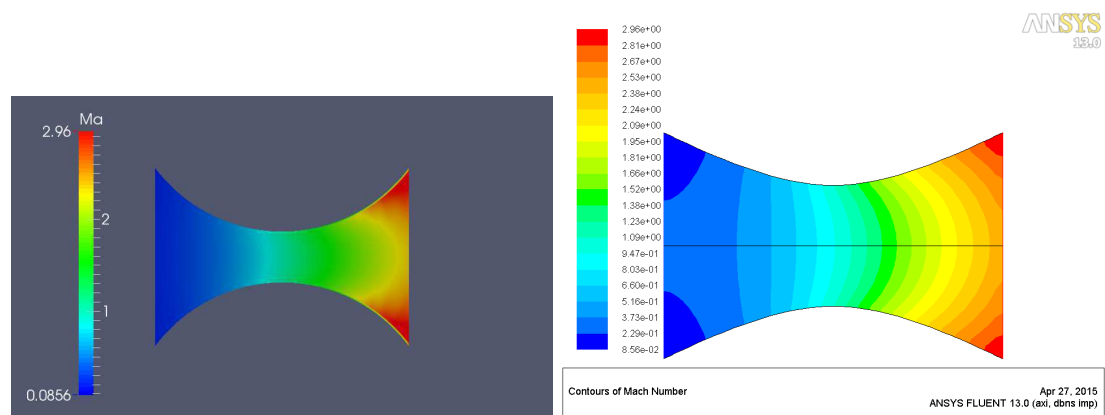


Figure 3.4: Mach number contours comparison between (a) rhoCentralFoam and (b) Fluent results. Both the solvers are being treated as inviscid.

we expect viscous effects to be confined to a very small region close to the wall. So it is reasonable to model the flow as inviscid and in both the *rhoCentralFoam* and Fluent solvers we have switched off solving viscous effects.

Figs 3.3 and 3.4 show the contours of pressure and Mach number. In each figure, (a) and (b) belong to rhoCentralFoam and Fluent results, respectively. Comparisons show very good agreement between both the inviscid solvers. Figure 3.5 shows the variation of (a) pressure, (b) Mach number along the centerline of a supersonic delaval nozzle. *rhoCentralFoam* results are found in excellent agreement with the fluent ones.

3.2 Validation with experimental data

Further, the *rhoCentralFoam* solver is validated with the experimental investigations of a thrust optimized contour nozzle [1]. Fig. 3.6 shows the boundaries of farfield where supersonic flow through nozzle and it's expansion into the atmosphere is investigated. For the

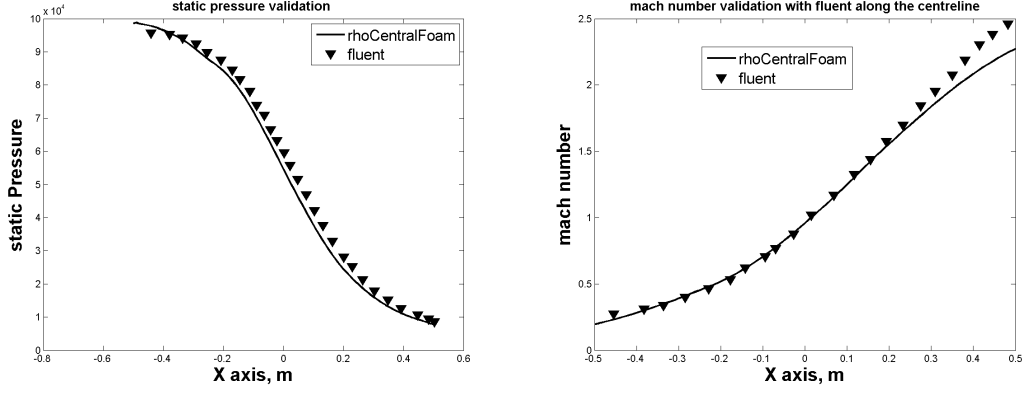


Figure 3.5: variation of (a) pressure, (b) Mach number along the centerline of a supersonic delaval nozzle. rhoCentralFoam is validated against Fluent and both the solvers are inviscid.

nozzle wall, no-slip and no-jump boundary conditions are implemented. Pressure farfields is used at the boundaries of computational domain and symmetry boundary condition is used for the axis. The viscosity in the present model is calculated using sutherland law:

$$\mu = \frac{A_s \sqrt{T}}{1 + T_s/T}$$

where the constants A_s and T_s are hard coded in the solver, Using $A_s = 4.458e-06$ and $T_s = 150.4$. The flow fields are computed by the steady Reynolds-Averaged NavierStokes (RANS) solver with SpalartAllmaras one-equation turbulence model. Schematic of thrust optimized contour nozzle [1] is shown in fig 3.6.

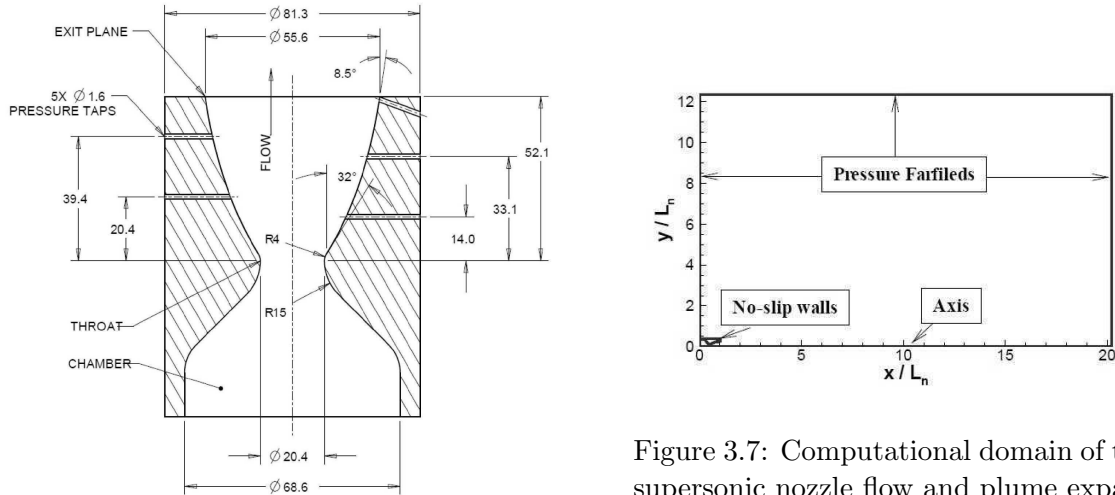


Figure 3.6: Schematic of thrust optimized contour nozzle [1].

Figure 3.7: Computational domain of the supersonic nozzle flow and plume expansion into the atmosphere. Farfield and wall boundaries are denoted and axis is symmetric.

Figure 3.7 shows the domain which covers a nozzle internal flow and the quiescent atmo-

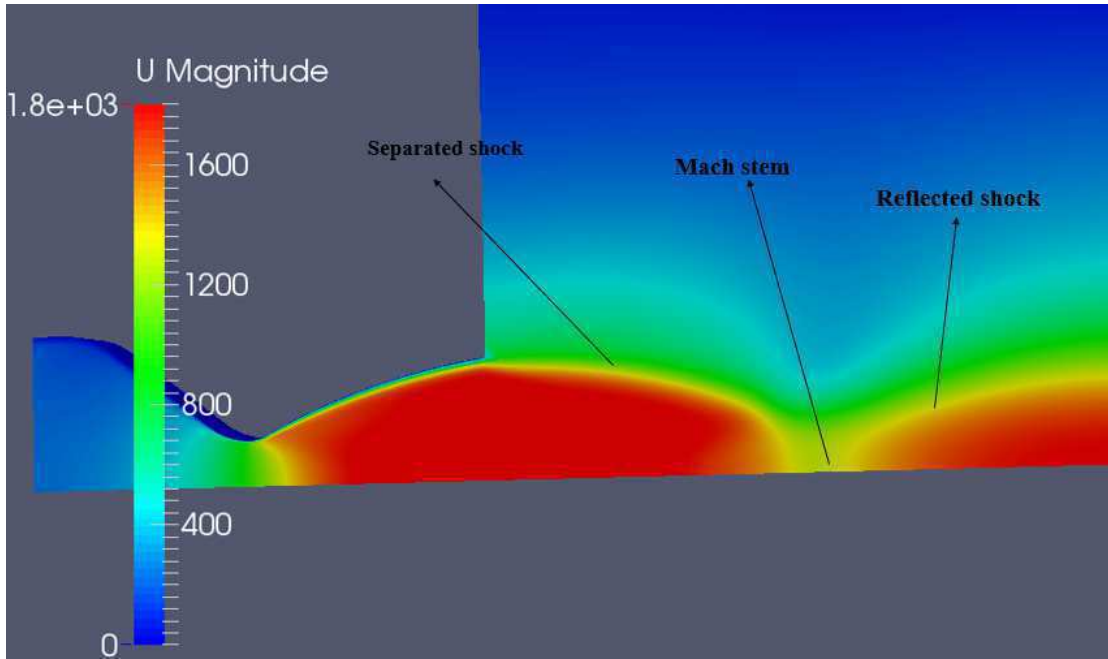


Figure 3.8: Visualization of mach stem (MS), reflected shock(RS), separated shock(SS) in the supersonic nozzle flow expansion.

sphere. Its size is sufficiently extended up to more than 12 and 20 times of a nozzle length in radial and axial direction, respectively, in order to impose farfield boundary conditions. Table 3.1 shows the properties for a decomposed gas of Hydrogen Peroxide

Thermochemical Properties	Values
Specific Heat	1.7242 kJ/(kg*K)
Specific Heat Ratio	1.2746
Prandtl Number	0.855
Molecular Weight	22.149 kg/kmole
Molecular Viscosity	0.4045 millipoise

Table 3.1: Chemical equilibrium properties for a decomposed gas of Hydrogen Peroxide [1]

Simulations are compared with the experimental data for two nozzle pressure ratio (NPR) conditions of 8 and 20 which are expected to cause the shock inside and outside the nozzle respectively. Simulations reported here are resulted from axisymmetric calculations. Fig 3.8 demonstrates velocity magnitude contours in the computational domain, which showcase mach Stem (MS), Reflected Shock(RS), Separated Shock(SS) phenomenon. Fig 3.9 shows the formation of shock inside the nozzle for NPR = 8.

Figure 3.10 shows the normalized centerline pressure variation along the axial distance for nozzle pressure ratio conditions of 8 and 20. *rhoCentralFoam* results exhibit good

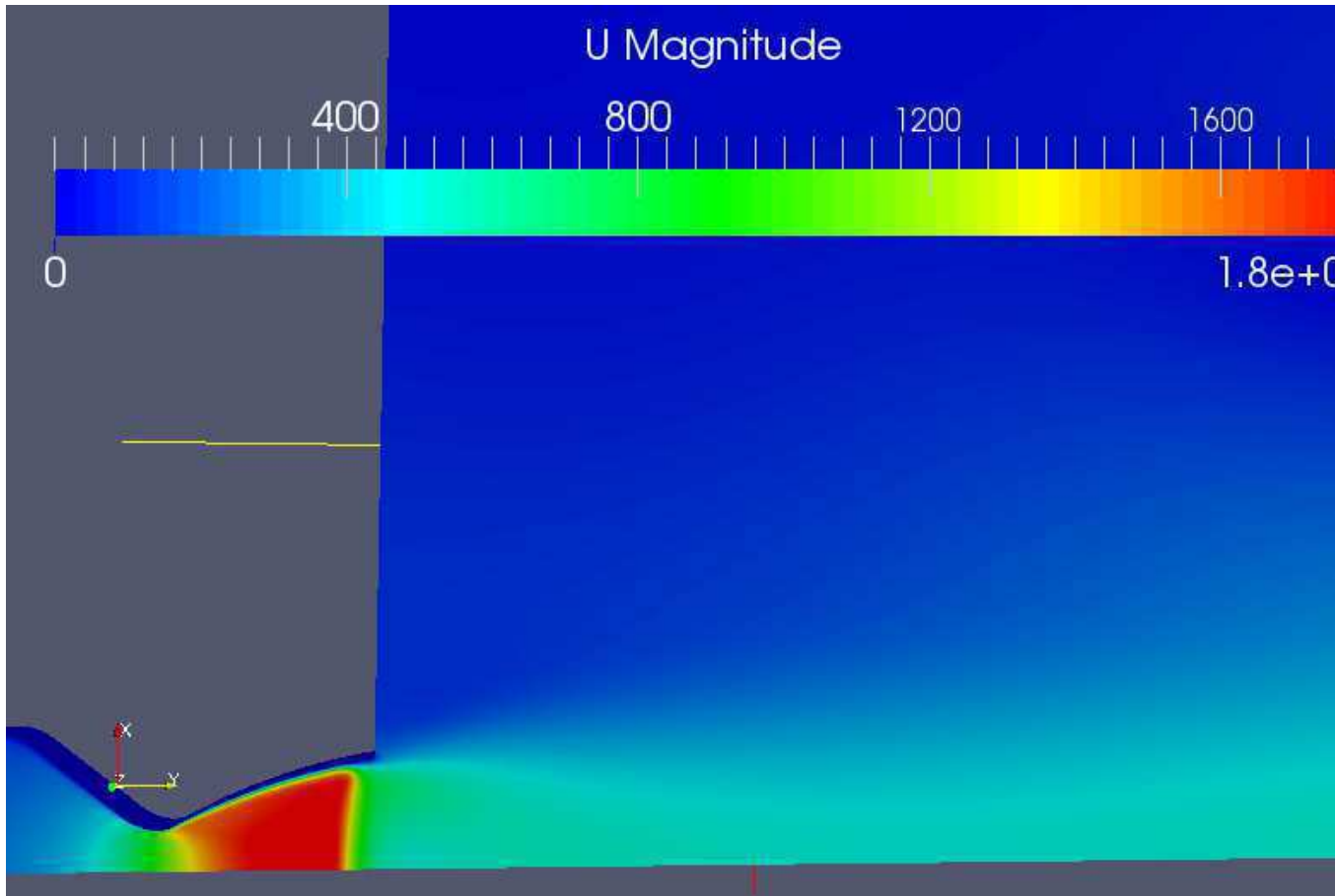


Figure 3.9: Visualization of the shock formed inside the nozzle.

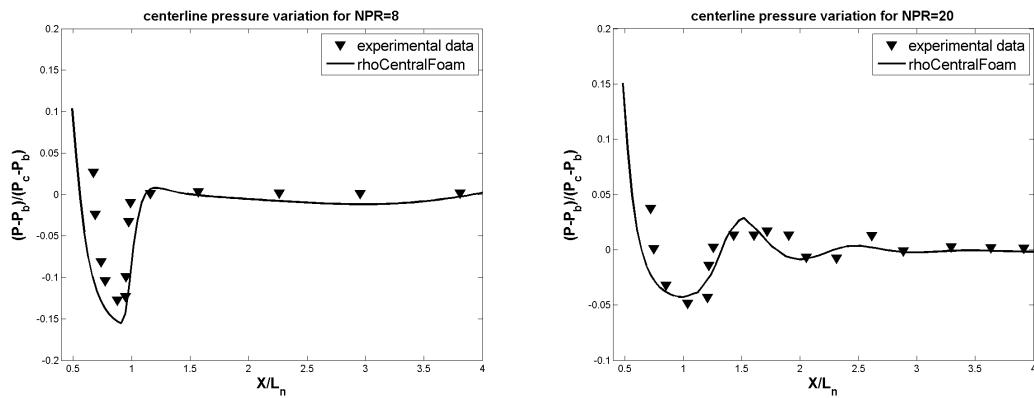


Figure 3.10: The normalized centerline pressure variation along the axial distance for rho-CentralFoam solver against the experimental data [1]. Results are presented for nozzle pressure ratio (NPR) (a) 8 and (b) 20.

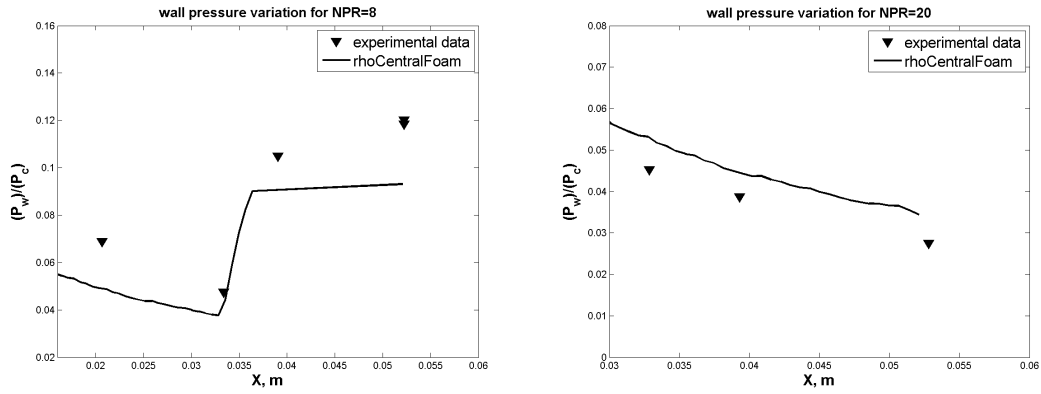


Figure 3.11: The normalized wall pressure variation along the axial distance for rhoCentralFoam solver against the experimental data [1]. Results are presented for nozzle pressure ratio (NPR) (a) 8 and (b) 20.

agreement with the experimental data. For $NPR = 8$, the shock is inside the nozzle and pressure remains approximately constant in the plume. While for $NPR = 20$, just outside the nozzle separation shock occurs followed by a mach stem (decrease in pressure) and then a weak reflected shock is observed (slight increase in pressure). Figure 3.11 shows the normalized wall pressure variation along the axial distance. *rhoCentralFoam* results show qualitative agreement with the experimental data. For $NPR = 8$, flow separation is noticed around $x = 0.035$ m. However, for $NPR = 20$, nozzle flow exhibit full expansion without any separation. The differences between the numerical and experiments may be attributed to roughness of the nozzle wall.

Chapter 4

Results and discussion for SHEFEX-III launcher

4.1 Closed interstage configuration

SHEFEX (Sharp Edge Flight Experiment) [33, 34] is a hypersonic research project initiated by German Aerospace Center (DLR) in 2002. The objective of this project is to investigate the hypersonic flight techniques with a re-entry vehicle launched by a sounding rocket. At present, DLR is working on the third experiment SHEFEX-III, and the selected launcher for SHEFEX-III is the Brazilian VLM-1 (Microsatellite Launch Vehicle-1) [2].

In the current investigation, we have selected the same launcher. The computational mesh is generated by the commercial software ICEM CFD [22], which is a CAD based grid generation package that supports multiblock structured, unstructured tetrahedral and unstructured hexahedral grids. Current mesh is composed of unstructured tetrahedral mesh. Free stream mach number is 2.6. Table 4.1 shows the test case conditions which have been used for the simulations. These conditions are similar to those at an altitude of 15.8 km.

Properties	Values
Pressure	10617.1 Pa
Temperature	216.650 K
Dynamic viscosity	0.143226 millipoise
Speed of sound	295.07 m/s
Density(ρ)	0.17072 kg/m ³

Table 4.1: Test case conditions

Figure 4.1 shows the computational domain for closed interstage configuration. Figs. 4.2 (a) and (b) show the coefficient of drag and coefficient of lift validation of *rhoCentralFoam* with Tau code [3, 4], for closed interstage respectively. The coefficient of drag (C_d) remains

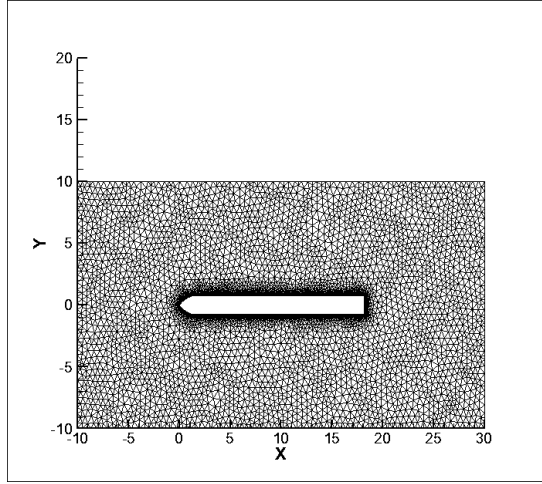


Figure 4.1: Computational domain for closed interstage configuration of VLM-1 (Microsatellite Launch Vehicle-1) [2].

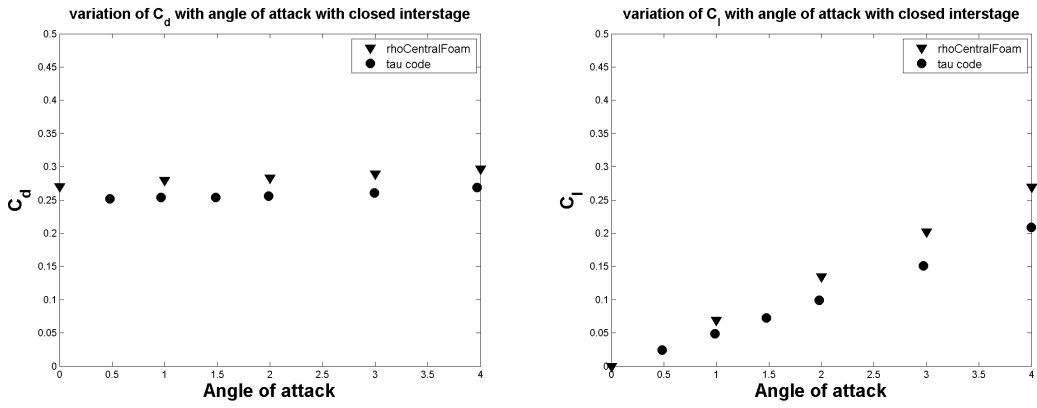


Figure 4.2: variation of (a) coefficient of drag (C_d) and (b) coefficient of lift (C_l) with angle of attack. *rhoCentralFoam* solver is validated against the results of Tau code [3, 4] for closed interstage configuration.

almost same with the increase in angle of attack whereas, the coefficient of lift (C_l) increases in direct proportion with the increase in angle of attack. *rhoCentralFoam* provide (C_d) results 5 % higher than the Tau code while the C_l results approximated by *rhoCentralFoam* are 15 % higher than the Tau code. The above mentioned variation can be attributed to approximated nose shape of VLM-1. The dimensions of the nose shape are not specified in the paper being validated [2]. The nose shape which we have used in our simulations is oogive nose shape.

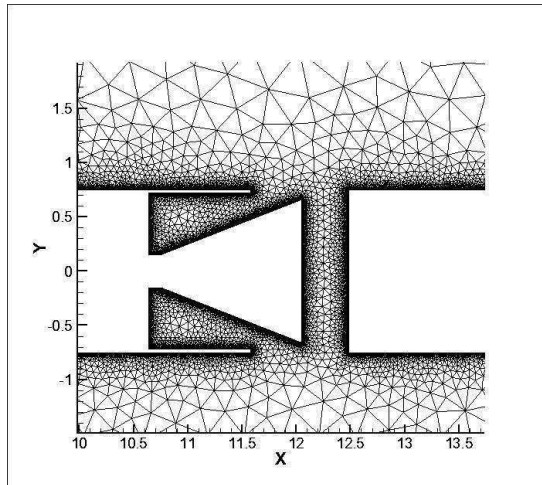


Figure 4.3: Close up view of the computational domain for open interstage configuration of VLM-1 (Microsatellite Launch Vehicle-1) with the nozzle being switched off [2].

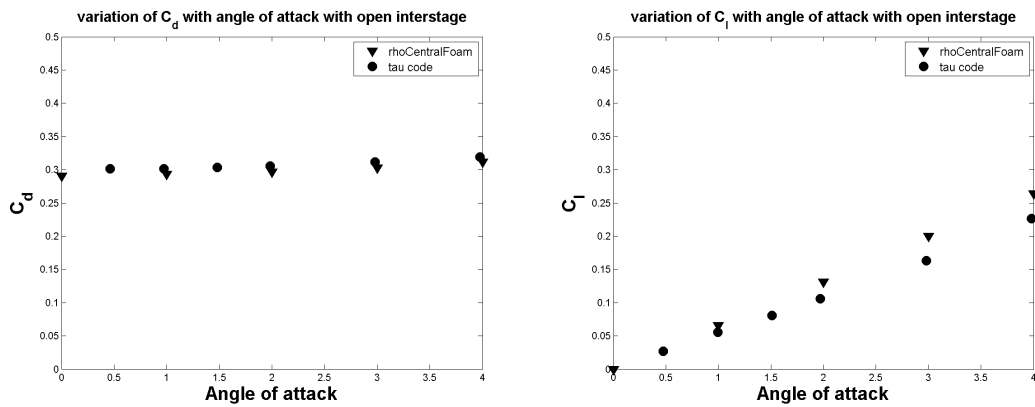


Figure 4.4: Variation of (a) coefficient of drag (C_d) and (b) coefficient of lift (C_l) with angle of attack. *rhoCentralFoam* solver is validated against the results of Tau code [3, 4] for open interstage configuration.

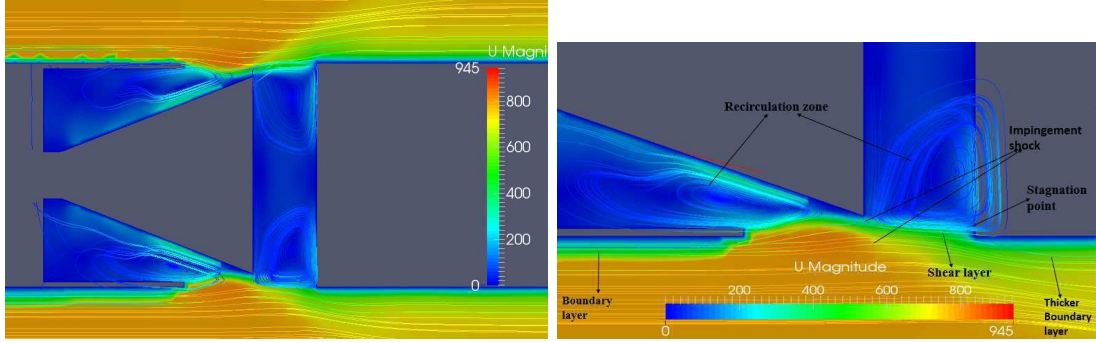


Figure 4.5: (a) Demonstration of the recirculation zones formed outside the nozzle and interior of aftwall for open interstage configuration. (b) Enlarged view of the recirculation zone show casing impingement shock, stagnation point and shear layer.

4.2 open interstage configuration with nozzle flow switched off

Figure 4.3 shows close up view of the computational domain for open interstage configuration of VLM-1 with the nozzle being switched off. Figs 4.4 (a) and (b) show the coefficient of drag and coefficient of lift validation of *rhoCentralFoam* with Tau code [3, 4], respectively for open interstage configuration. With the open interstage configuration C_d results approximated by *rhoCentralFoam* are in very good agreement with the Tau code. It can be noticed that C_d remains almost same with the increase in angle of attack whereas, C_l increases with increase in angle of attack. However, the difference in the results provided by *rhoCentralFoam* and Tau code is also less when compared to close interstage configuration.

At small angles-of-attack, the application of a open inter-stage structure will increase the drag coefficient of the rocket by 20 % in comparison to closed interstage configuration. However, this effect on lift coefficient is insignificant. The increased drag is mainly caused by the additional wave drag induced by the open inter-stage structure. The flow in the inter-stage cavity is unsteady, which may effect the flight path of the rocket.

Figure 4.5 shows the recirculation zones formed with open interstage configuration. The flow at the open inter-stage section is an axisymmetric open cavity flow (the classification of cavity flow can be seen in Ref. [35]) distorted by the nozzle wall in the cavity: a shear layer is formed to divide the supersonic free stream flow and the subsonic flow in the cavity. In addition, we can also notice the thicker boundary layer, recirculation zones, impingement shock and stagnation point.

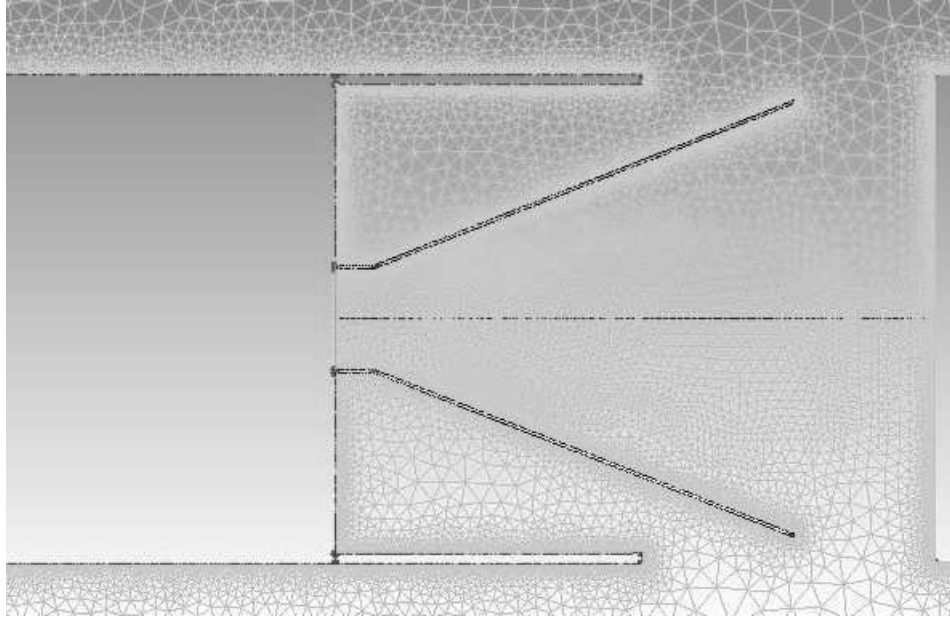


Figure 4.6: Shefex-III Launcher mesh with nozzle flow switched on and the close up view of computational domain around the nozzle.

4.3 open interstage configuration with nozzle flow switched on

The next study is open interstage configuration with nozzle flow switched on. Free stream conditions are similar to the previous case. For the nozzle flow, choked condition is taken as an assumption. The exit area to throat area ratio of the nozzle is 18.13. Stagnation pressure and stagnation temperature at the nozzle inlet is $3.66 * 10^6$ Pa and 1200 K, respectively. All simulations are carried upto $t = 0.0131$ seconds(s) as at $t = 0.013$ s the forces on the two stages are balanced [20]. After $t = 0.0131$ s the 2^{nd} -stage gets positive axial force i.e. it can be accelerated. Theoretically, at $t = 0.0131$ s the two stages can be disconnected and after that the 2^{nd} -stage-motor has the ability to separate the two stages. In the Current investigation various plume deflector configurations like conical, spherical and blunt are simulated. Heat transfer, pressure and friction coefficients are reported on critical surfaces which are the top of first stage, outer surface of the second stage nozzle wall and interior of second stage aftwall.

Figure 4.6 shows the computational domain with the nozzle flow switched on along with the external freestream flow. Three plume deflector configurations are shown in Fig 4.7 (a) blunt, (c) conical and (e) spherical. In these sub-plots, top surface of first stage, nozzle wall of second stage and region 'a', i.e. interior of aftwall are clearly demonstrated and arc lengths for each of these surface are also mentioned in Fig. 4.7 (e).

Figures 4.7 (b), (d) and (f) shows the velocity contours in the entire computational

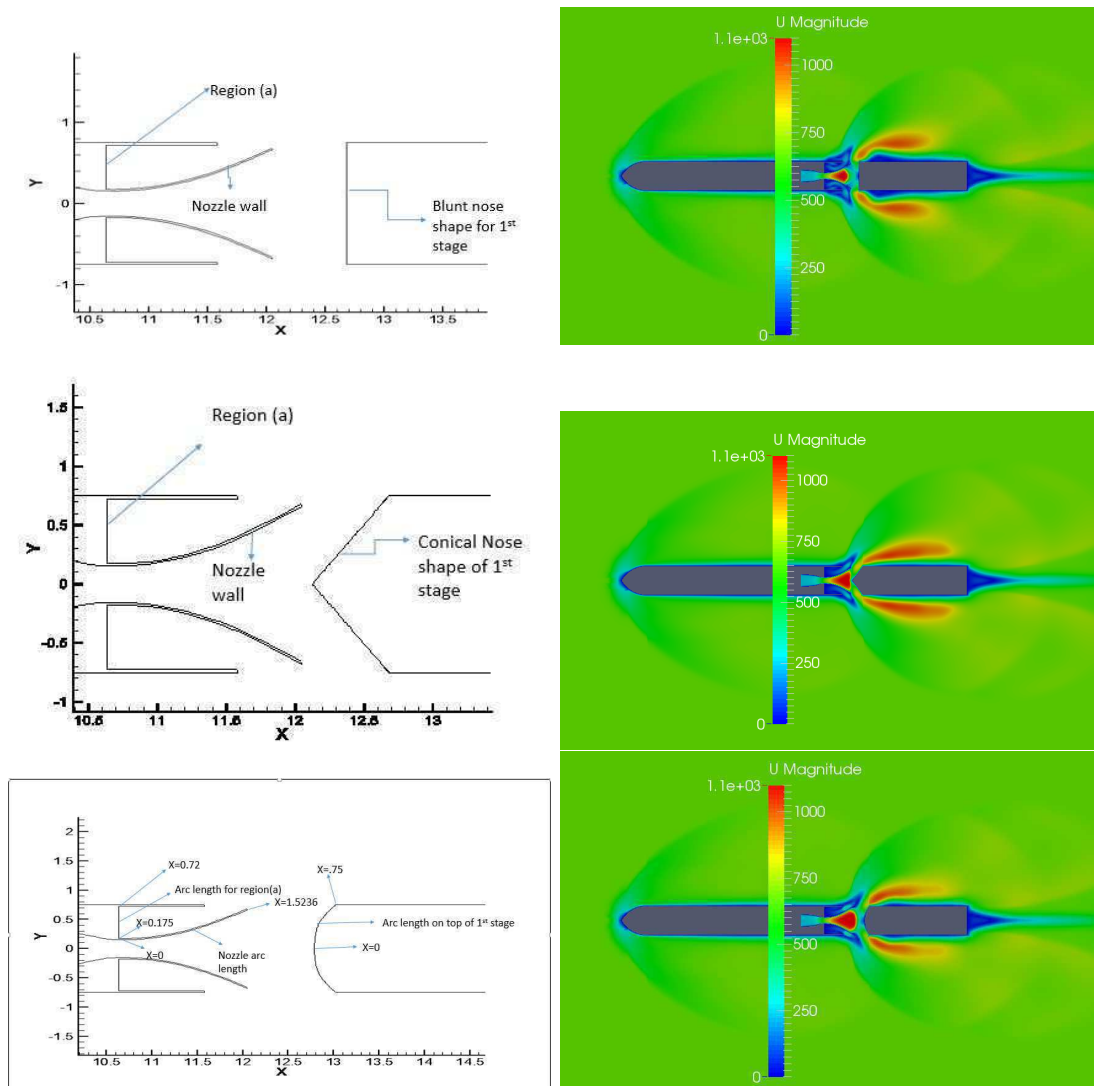


Figure 4.7: Left side plots: (a), (c) and (e) show schematic computational domains of stage separation studies with blunt, conical and spherical plume deflector configurations, respectively. Right side plots: (b), (d) and (f) demonstrate velocity contours for blunt, conical and spherical configurations, respectively.

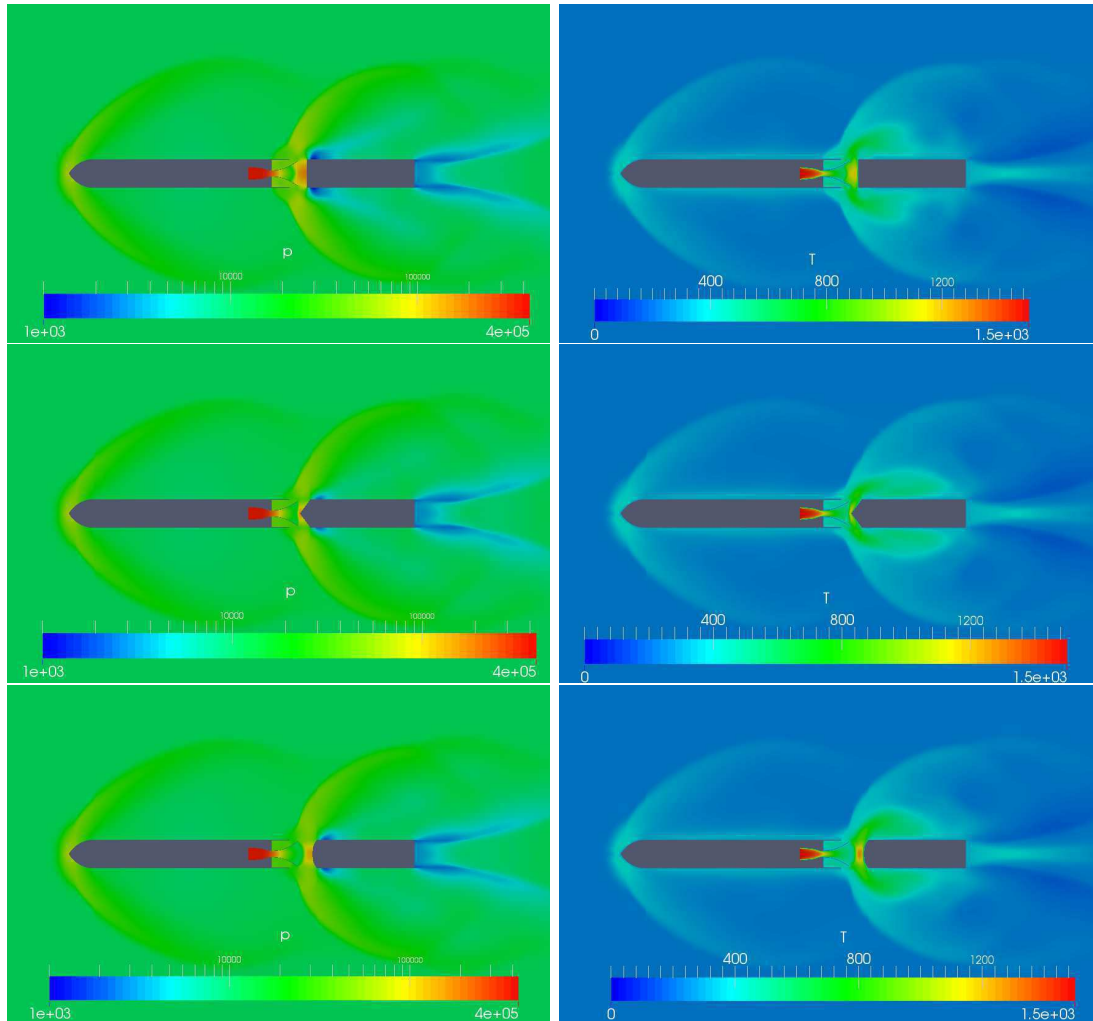


Figure 4.8: Left side plots show pressure contours while the right side ones demonstrate temperature contours for (a) & (b) blunt, (c) & (d) conical and (e) & (f) spherical plume deflector configurations.

domain for blunt, conical and spherical configurations, respectively. In all cases, a normal shock appears near the nozzle exit and an expansion wave forms along the lower stage through which the compressed gas expands into the atmosphere. It also demonstrates that the obstacle effect of the vented plume on the free-stream is reduced with the spherical and conical plume deflectors in comparison to a blunt one. The ‘separation shock’ is weaker in conical and spherical deflectors. In addition to this, the separation distance of the boundary layer on the aft wall of the 2nd-stage is reduced with conical and spherical deflectors compared to the blunt deflector.

Figures 4.8 : (a), (c) and (e) show the pressure contours in the blunt, conical and spherical configurations, respectively. It can be noticed that a stagnation point exists at the intersection of the plume axis with the surface coinciding with a maximum pressure. The

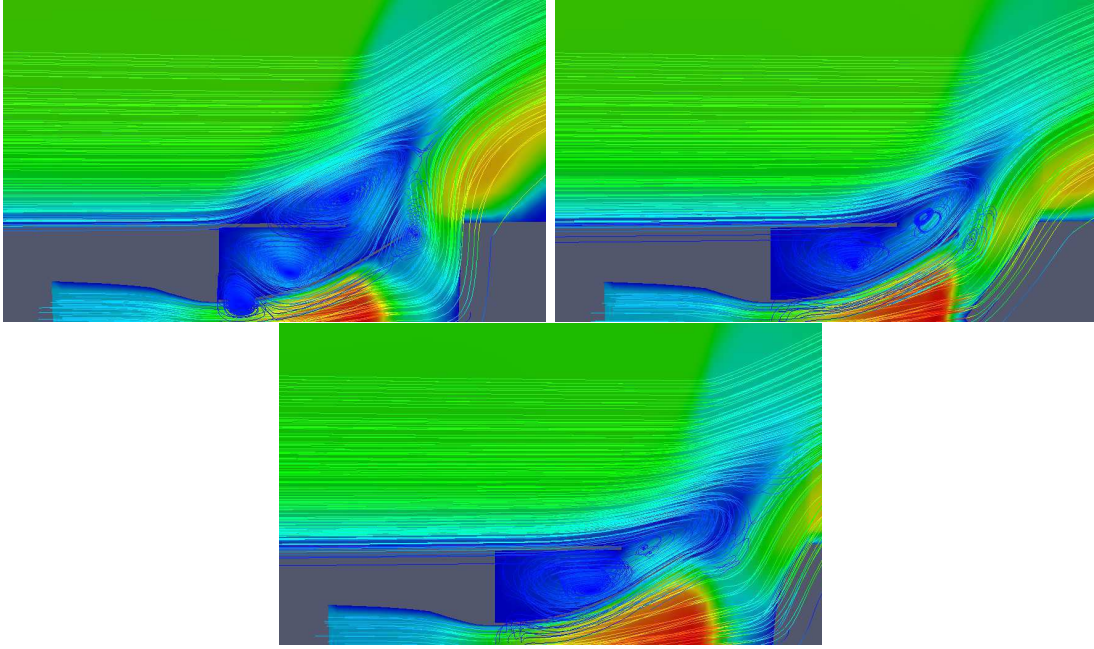


Figure 4.9: Zoomed view of velocity contours to show case plume interaction with supersonic freestream and key recirculation zones for (a) blunt, (b) conical and (c) spherical plume deflector shapes.

flow around the stagnation point is subsonic and it is supersonic in rest of the computational domain. Figs 4.8 : (b), (d) and (f) show the temperature contours in the blunt, conical and spherical configurations, respectively. High temperature zone on the top of first stage surface is smaller for conical deflector while compared to spherical and blunt ones.

Figures 4.9 : (a), (b) and (c) showcase zoomed view of velocity contours demonstrating plume interaction with supersonic freestream and key recirculation zones. In all three plume deflector configurations, a common recirculation zone exists between the interior of aft skirt and the outer nozzle wall of 2^{nd} stage. However, in conical and blunt configurations, an additional recirculation zone can be observed around the nozzle wall at exit location. However, in conical configuration it moves away from the nozzle exit location. This recirculation region can cause serious heating of the outer nozzle wall near the exit. In blunt configuration two additional recirculation regions are found, one near the wall joining of aft skirt and outer nozzle wall i.e. near region ‘a’ and the other at the outer wall of aft skirt. These can result in increased temperature of the aft skirt and region ‘a’ which can be hazardous for the successful flight operation. There are no such recirculation zones observed in conical and spherical configuration. It can be noticed that a separation shock occurs in all the configurations which is formed due to the interaction of the free stream flow with the nozzle flow. This separation shock moves toward the 2^{nd} stage in case of blunt deflector. Also, the separation distance of the boundary layer on the aft wall of the

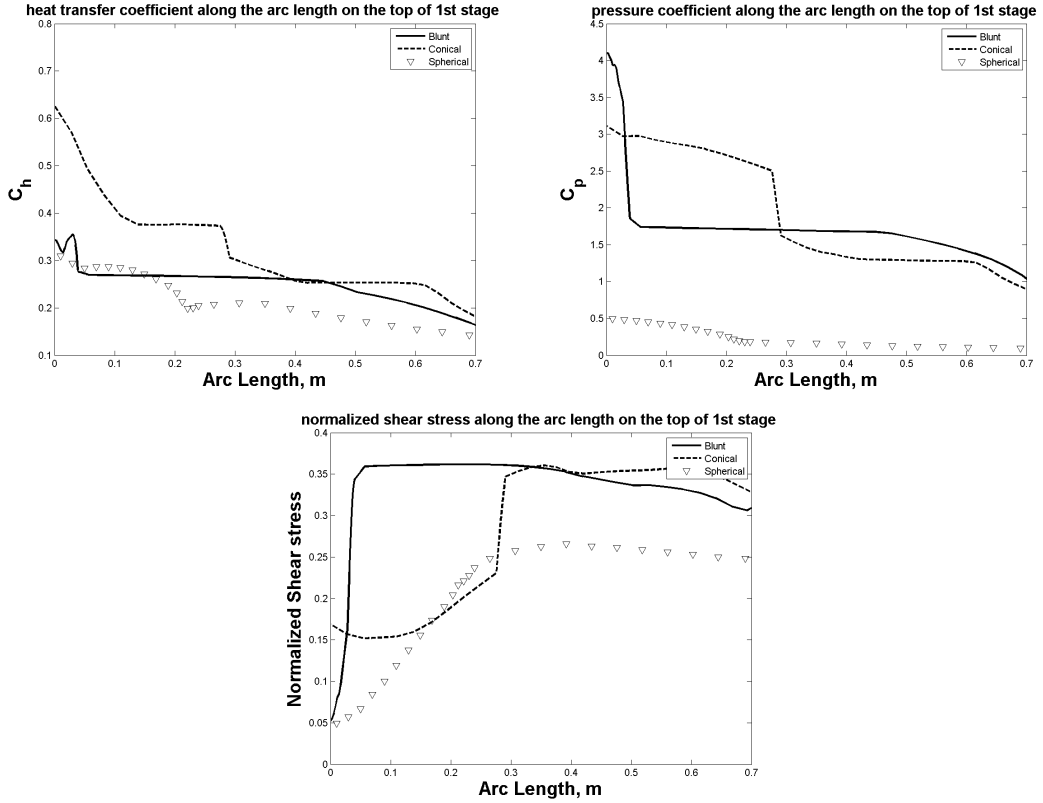


Figure 4.10: Variation of aero-thermodynamic coefficients on the top of 1st stage surface along the arc length and comparison between three different plume deflector shapes. Here, (a) heat transfer coefficient (C_h), (b) pressure coefficient (C_p) and (c) normalized shear stress.

2nd-stage is reduced with conical and spherical deflectors compared to the blunt one. The contours show that the impingement shock is formed inside the nozzle for blunt and conical configuration, it is formed at the nozzle exit for spherical one.

Fig 4.10 (a) shows the comparison of wall heat flux on top of 1st stage surface normal to the nozzle exit. Heat transfer coefficient is minimum for the spherical while it is maximum for the conical. The point of maximum heat flux is also observed in conical configuration, which is analogical to the experimental investigation done by Lengrand et al. [36]. C_h for all the configurations decreases with increase in arc length. It is minimum at the point farthest from the center i.e. arc length = 0.7 m for all configurations. This is due to the cooling effect of the ambience (216.65 K) which is far below the temperature of the plume emitted by nozzle (1500 K). This cooling effect is missing at the center of 1st stage which results in highest value of C_h at the center i.e. arc length = 0. Fig. 4.10 (b) shows the comparison of pressure coefficient (C_p) on the top of first stage. C_p for the blunt configuration decreases suddenly, then remains constant and then again decreases. C_p is minimum for spherical configuration. For the conical configuration, it can be observed that C_p decreases slowly

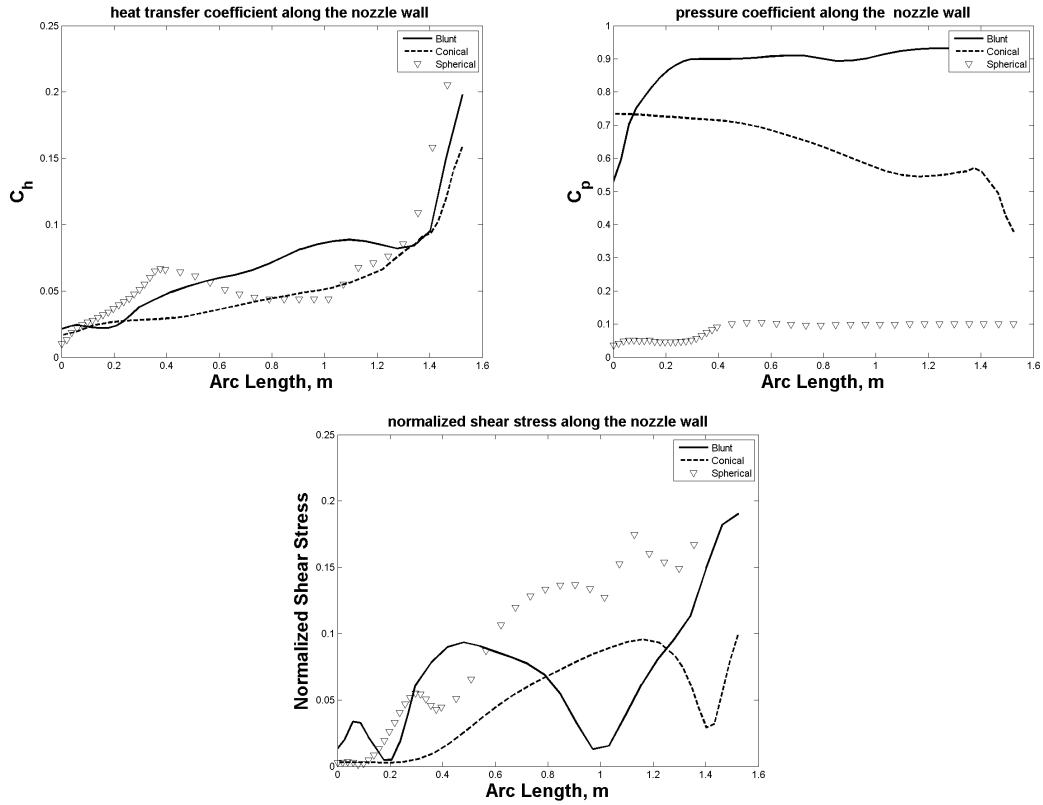


Figure 4.11: Variation of aero-thermodynamic coefficients on the outer nozzle wall along the arc length and comparison between three different plume deflector shapes. Here, (a) heat transfer coefficient (C_h), (b) pressure coefficient (C_p) and (c) normalized shear stress.

first and then sharply. It can be stated that in all configurations, there is a decrease in C_p which shows expansion. However, weak shock waves can be observed in conical and blunt deflectors indicated by small rise in C_p . For spherical configuration no shock is observed as this shape allows the nozzle flow to expand freely into the bulk stream. Fig. 4.10 (c) shows the normalized shear stress on top of 1st stage surface normal to the nozzle exit. It can be observed that there is sharp rise in blunt configuration which indicates sudden fall in pressure. At arc length = 0, normalized shear stress for conical case is highest, which then decreases. This indicates a very small high temperature zone for conical configuration as compared to spherical and blunt case. For spherical, normalised shear stress increases gradually and approaches a sigmoid curve.

Fig 4.11 demonstrates the variation of aero-thermodynamic coefficients on the outer nozzle wall surface along the arc length and comparison between three different plume deflector shapes. In Fig 4.11 (a) heat transfer coefficient (C_h) increases as we move towards the nozzle exit. The sudden rise of C_h after arc length = 1.2 m can be attributed to the recirculation zone found near nozzle exit which results in enhanced heat transfer, for all three configurations. In Fig. 4.11 (b), a sudden rise in pressure coefficient (C_p) can be

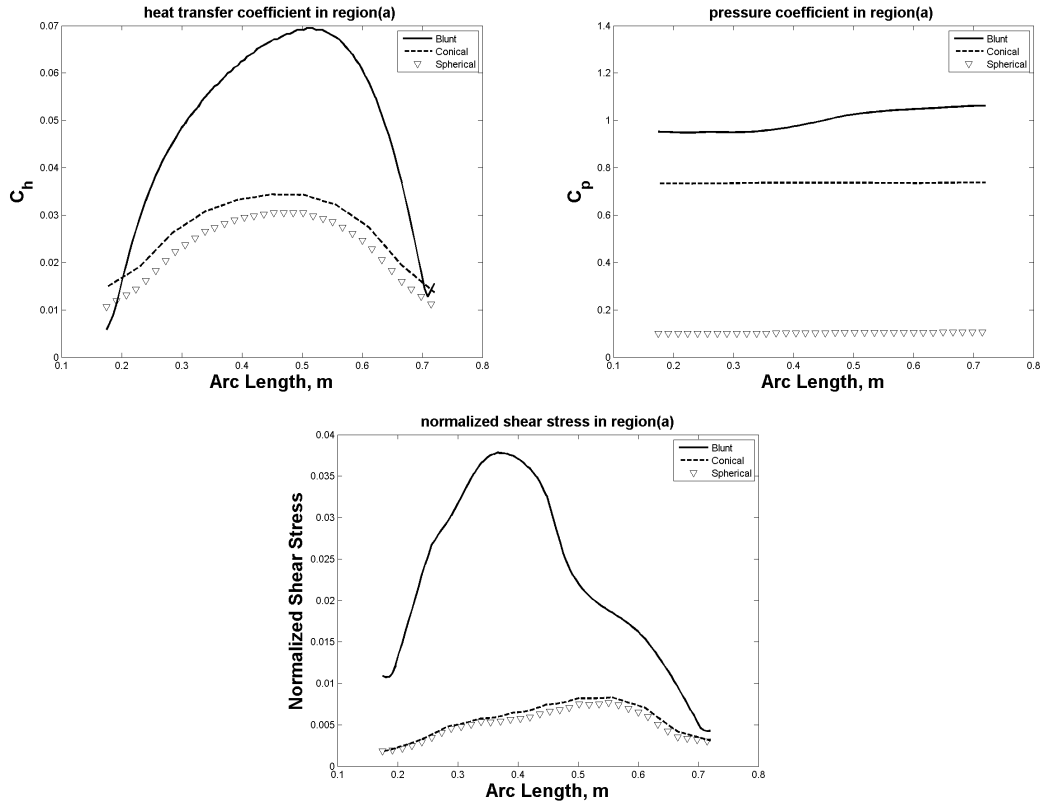


Figure 4.12: Variation of aero-thermodynamic coefficients on the interior of aftwall i.e. region ‘a’ along the arc length and comparison between three different plume deflector shapes. Here, (a) heat transfer coefficient (C_h), (b) pressure coefficient (C_p) and (c) normalized shear stress.

observed for blunt case between arc length 0 m to .2 m i.e. near the throat of nozzle, which shows the formation of a strong shock wave. For conical configuration, C_p decreases gradually as we move away from throat which implies the presence of expansion fan. At arc length = 1.2 m, rise in C_p for conical case can be observed which indicates a weak shock and this shock is weakest in spherical configuration. In Fig. 4.11 (c) normalized shear stress for spherical configuration is higher as compared to conical and blunt which may pose problems due to unexpected turning moments. Even though shear stress is very small as compared to pressure, it cannot be neglected as not only the forces but also the turning moments which often pose problems. For spherical configuration, pressure on the outer nozzle wall is lowest which implies that the normalized shear stress should be highest and it is clearly visible in Fig. 4.11 (c).

Figure 4.12 showcase, variation of aero-thermodynamic coefficients along the arc length, on the interior of aftwall i.e. region ‘a’. In Fig. 4.12 (a) the location of maximum heat transfer coefficient (C_h) corresponds to the position of the reattachment point i.e. arc length = 0.55 m. This is due to an additional recirculation zone formed with the blunt case, there is an enhancement in the heat transfer. In Fig. 4.12 (b) pressure coefficient (C_p) for blunt

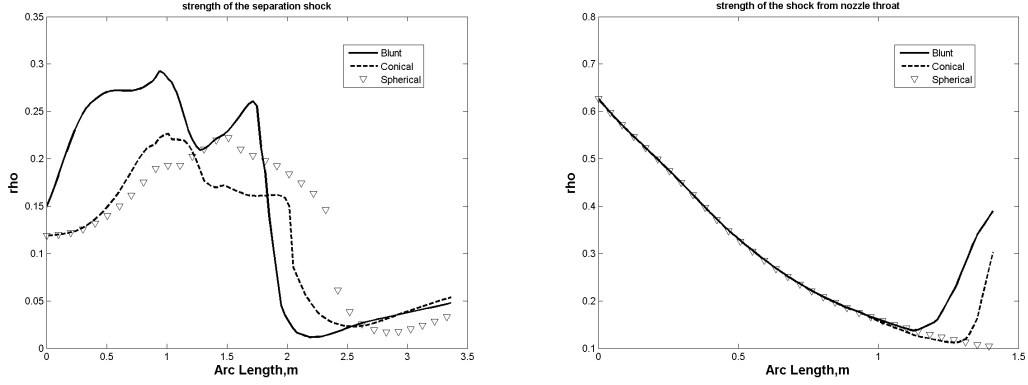


Figure 4.13: (a) The density variation on the outersurface of aftwall. (b) The centerline density variation inside the nozzle starting from throat to the exit. Comparisons are made between three plume deflector shapes.

case increases gradually between arc length 0.3 m to 0.5 m which shows the formation of weak shock wave. For conical and spherical configuration, neither shock wave nor expansion is found. In Fig. 4.12 (c) normalized shear stress for blunt configuration is the highest, this may result in uneven turning moments. As compared to the outer nozzle wall, the order of magnitude of normalized shear stress on aftwall is very small.

Figure 4.13 (a) show case the density variation on the outer surface of aftwall. It can be observed that there are steep slopes in blunt configuration in comparison to conical and spherical deflectors. Hence, it can be stated that the strengths of separation shock is strongest for the blunt case, they are weakest for conical and spherical configuration. Fig 4.13 (b) shows the centerline density variation inside the nozzle starting from throat to the exit. It can be noticed that the impingement shock for conical and blunt configuration is formed inside the nozzle, while the shock is formed outside the nozzle exit for spherical deflector. The impingement shock is formed in further upstream for the blunt configuration compared to conical case, as we move from nozzle throat to exit.

4.3.1 Parametric study for various cone angle configurations

The *rhoCentralFoam* solver is further used to simulate the test case for conical deflector with cone angles of 22° , 33° , 54° and 60° . All other test conditions are identical to the one described in the previous section.

Figure 4.14 showcases the zoomed view of velocity contours to demonstrate plume interaction with supersonic freestream and key recirculation zones for conical deflector with cone angles of (a) 22° , (b) 33° , (c) 54° and (d) 60° . For all configurations, a common recirculation zone persists between the interior of aft skirt and outer nozzle wall. Recirculation region around the tip of nozzle wall at exit location is also observed in all the configurations.

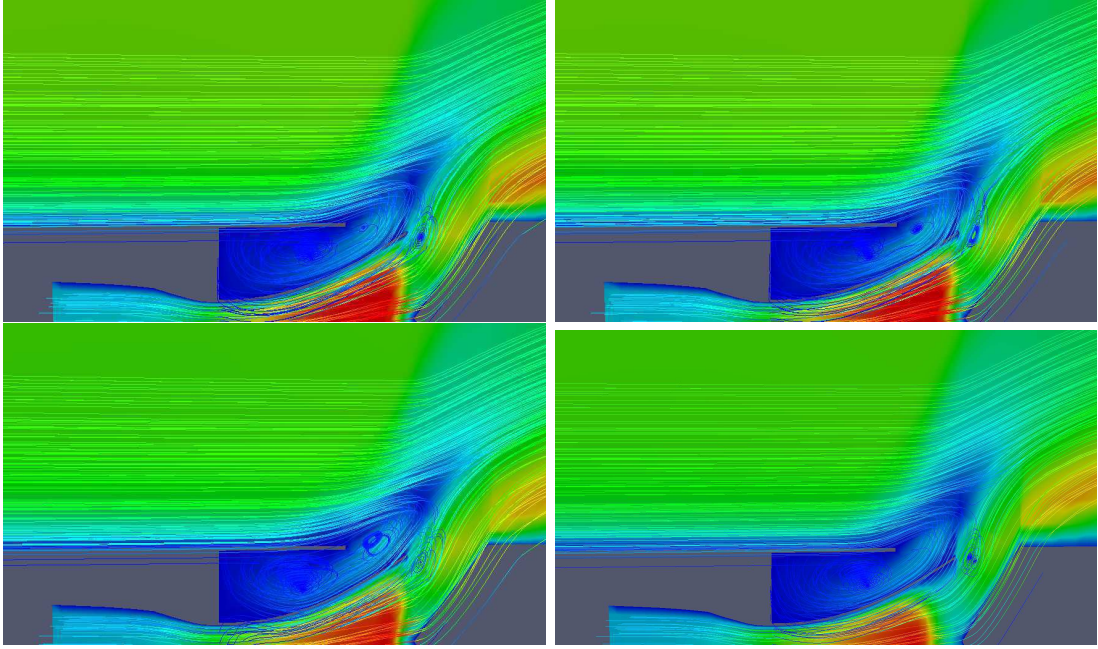


Figure 4.14: Zoomed view of velocity contours to demonstrate plume interaction with supersonic freestream and key recirculation zones for conical deflector with cone angles of (a) 22° , (b) 33° , (c) 54° and (d) 60° .

It is found to be very faint for 54° , while significant for 33° and 60° . This region can cause overheating of the tip of nozzle wall at exit location. Near the end of the aft skirt, a weak recirculation region is observed for 22° , a stronger in case of 33° and a strongest one is observed in case of 54° while there is no such recirculation region noticed in case of 60° . It can be seen that the impingement shock moves toward the nozzle throat with the increase in the cone angle. The separation shock also follows the same trend and with the increase in the cone angle, it moves towards the 2^{nd} stage.

Figure 4.15 demonstrates the variation of aero-thermodynamic coefficients on the top of 1^{st} stage surface along the arc length and comparison between various cone angles of 22° , 33° , 54° and (d) 60° . As observed in Fig. 4.10 (a) maximum C_h is found at the center i.e. arc length = 0, while minimum is observed at the farthest point from the center, which is due to the cooling effect of free stream. The point of maximum C_h is observed for 60° and minimum for 33° and 22° . Pressure coefficient (C_p) decreases for all configuration along the arc length, which shows expansion. The steep slopes in C_p can be attributed to the reflection of flow from region 'a'. Steep slope of normalized shear stress is noticed for 22° , which is due to high velocity gradients along the arc length.

Fig 4.16 demonstrates the variation of aero-thermodynamic coefficients on the outer nozzle wall along the arc length and comparison between various cone angles 22° , 33° , 54° and 60° . In plot (a) maximum heat transfer is observed for 22° configuration i.e. the nozzle is most vulnerable to overheating among all the cone angles. However, C_h is least

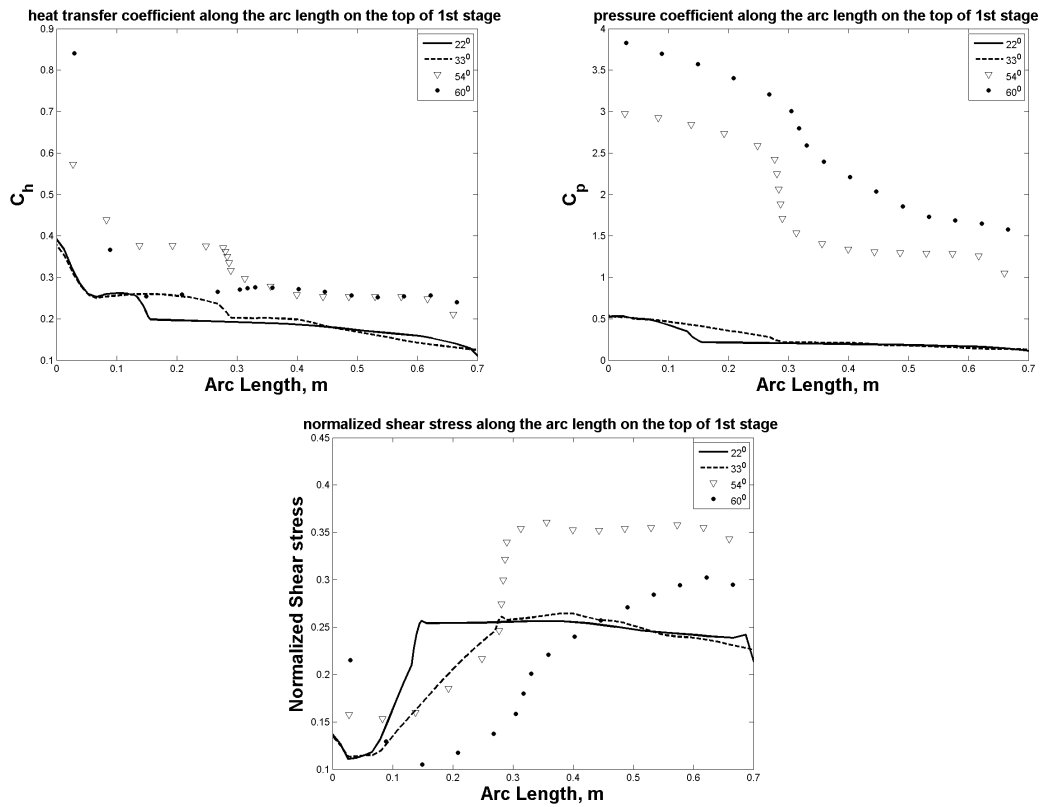


Figure 4.15: Variation of aero-thermodynamic coefficients on the top of 1st stage surface along the arc length and comparison between various cone angles of 22° , 33° , 54° and 60° . Here, (a) heat transfer coefficient (C_h), (b) pressure coefficient (C_p) and (c) normalized shear stress.

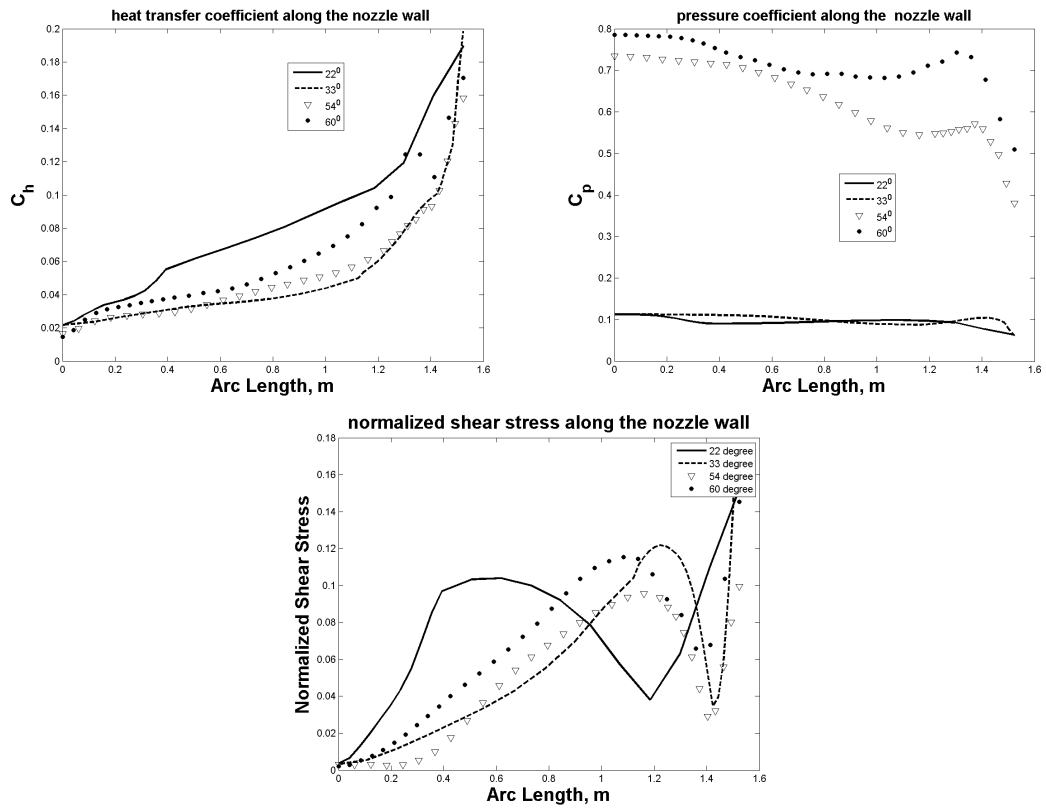


Figure 4.16: Variation of aero-thermodynamic coefficients on the outer nozzle wall along the arc length and comparison between various cone angles 22° , 33° , 54° and 60° . Here, (a) heat transfer coefficient, (b) pressure coefficient and (c) normalized shear stress.

for 54° and 33° configuration. Sharp rise of C_h at the nozzle exit can be attributed to the recirculation zone observed near the nozzle exit which causes enhanced heat transfer. It is usual that C_h should increase with the increase in cone angle. For 22° and 33° maximum amount of plumes diffuses into the free stream, downstream to the nozzle wall, while for 60° the diffusion is upstream to the nozzle exit wall. However for 54° configuration which is in between the above mentioned cone angles, a large portion of plumes enter the cavity between nozzle wall and aft skirt i.e for this case velocity of plumes in the cavity is maximum. The velocity is lower for 33° and lowest for other configurations. It has been found in the literature that the separation of flow around sharp corners and turns increases with the increase in the reynolds number i.e. velocity. Hence the separation is maximum for 54° when it moves along the nozzle wall near exit location (a sharp turn) and near the throat of nozzle wall (a sharp corner). For 60° , the amount of plumes entering the nozzle wall is reduced as maximum portion of it, is diffused into the freestream upstream to nozzle wall i.e. reynolds number will be low which implies that the separation will be also low around the sharp corners. For 22° , the amount of plumes entering is less i.e. less separation, in comparison to 54° , 60° and 33° . which can be seen by high values of C_h . Initially, for all configurations as we move away from throat C_p decreases which indicate expansion (see Fig (b)). At arc length = 0.4 m a very weak shock is observed for 22° , a weak shock for 33° at 1.25 m, a strong shock for 54° at 1.2 m and a strongest one for 60° at 1 m. These shocks may be formed due to the reflection of flow from region 'a'. As the plumes will be flowing from the nozzle exit wall towards the throat. So, if we move along the plot from arc length = 1.52 m towards arc length = 0 m. It can be observed that a sharp slope exist for 54° and 33° between arc length 1.4 m to 1.52 m and gradual slope for 22° . This implies that the separation of flow is significant in 54° and 33° around the nozzle exit wall and minimum for 22° . Hence C_h along the nozzle wall is highest for 22° and minimum for 54° and 33° . However, a sudden drop in C_h can be observed for 22° between arc length 0 m and 0.4 m. This is again due to the separation near the sharp corner joining nozzle wall and region 'a'. High normalised shear stress regions can be found near the nozzle exit i.e. after arc length 1.2 m (see Fig (c)).

Fig 4.17 demonstrates the variation of aero-thermodynamic coefficients on the interior of aftwall i.e. region 'a' and comparison between various cone angles. It can be observed that the maximum C_h value increases with increase in cone angle until 54° and then shows a decreasing trend for 60° at arc length = .45 m. This is due to the reattachment that takes place in region 'a' for 54° configuration. The reduced separation can be seen by high value of C_h at arc length = 0.15 m to 0.2 m and also after arc length of 0.65 m for 60° . There are neither expansion fans nor shock waves as C_p remains constant for all cone angles. The peak of maximum normalised shear stress configuration is shifted slightly towards the aft skirt for 54° , while other configurations attain the peak at a common point along the arc length i.e. 0.45 m. Near the point joining outer nozzle wall and region 'a', normalized shear

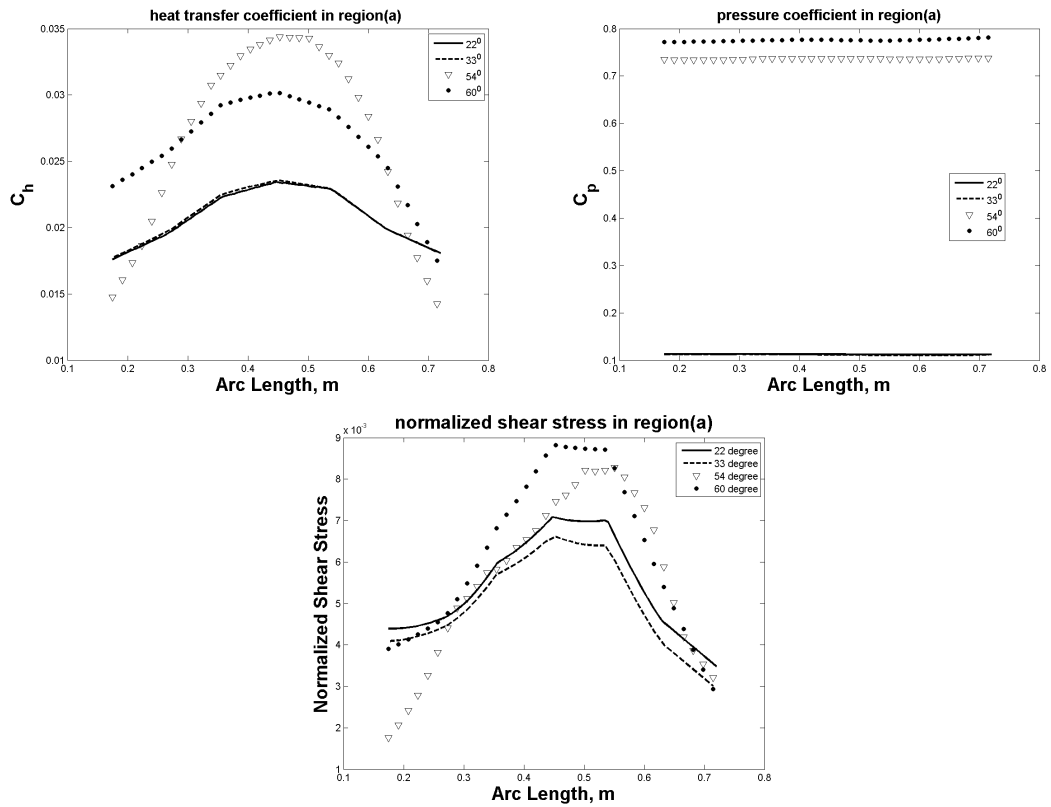


Figure 4.17: Variation of aero-thermodynamic coefficients on the interior of aftwall i.e. region 'a' and comparison between various cone angles of 22°, 33°, 54° and 60°. Here, (a) heat transfer coefficient (C_h), (b) pressure coefficient (C_p) and (c) normalized shear stress.

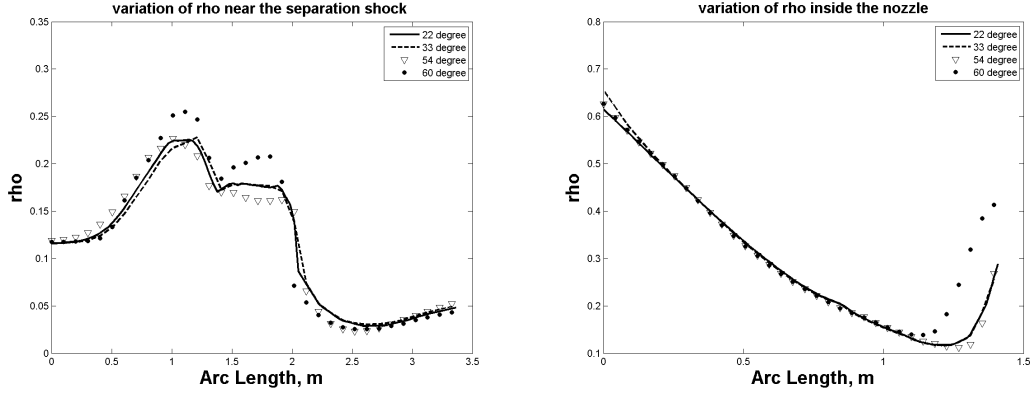


Figure 4.18: (a) The density variation on the outersurface of aftwall (b) The centerline density variation inside the nozzle starting from throat to the exit. Comparisons are made between various cone angles of a conical plume deflector shape.

stress is minimum for 54^0 . It can be stated that normalized shear stress first decreases with increase in cone angle until 33^0 and then increases with increase in cone angle.

Figure 4.18 (a) shows the density variation on the outersurface of aftwall. Steep slopes can be observed for 60^0 cone angle which states that the strength of separation shock is strongest for this case in comparison to other cone angles. Weak shock waves can be observed for other cone angles. Fig 4.18 (b) shows that the centerline density decreases inside the nozzle as we move from throat to the exit. This shows that the flow is being accelerated. Impingement shock is formed earlier in 60^0 while, for other cone angles the shock is formed at a later distance.

4.3.2 Parametric study for various separation distances with cone angle of 54^0

Figure 4.19 demonstrate the zoomed view of velocity contours to demonstrate plume interaction with supersonic free stream and key recirculation zones for conical deflector with separation distances of (a) $(1/16)D$, (b) $(1/8)D$, (c) $(1/4)D$ and (d) $(1/2)D$ between 1st stage and second stage, where D is the nozzle diameter. A common recirculation zone occurs between the interior of aft skirt and outer nozzle wall in all conical configurations with varying separation distances between 1st stage and 2nd stage. However, it is very faint when the separation distance is $(1/2)D$. It can be stated that the common recirculation zone fades away with the increasing separation distance. The recirculation regions found near the nozzle exit and the aft skirt also seems to follow the same trend i.e. becomes faint with the increasing separation distance. It can be noticed that the impingement shock moves toward the nozzle exit as the separation distance is increased. For $(1/2)D$, the impingement shock is formed outside the nozzle while, for $(1/4)D$, it is formed just at the nozzle exit. The separation shock moves away from the 1st stage as the separation distance is being

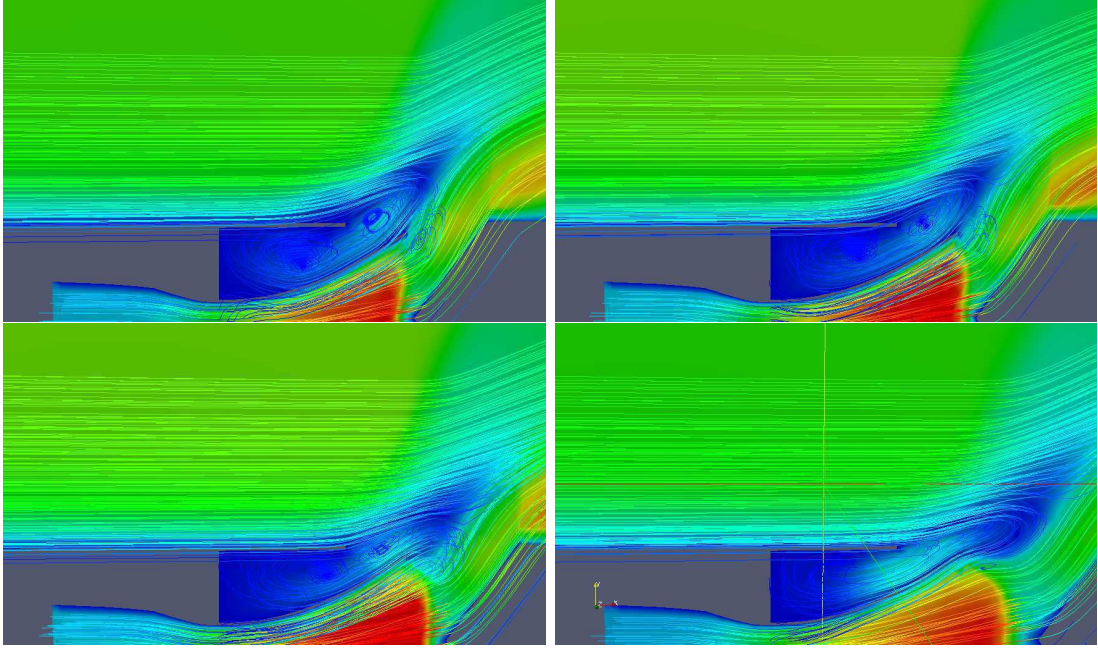


Figure 4.19: Zoomed view of velocity contours to demonstrate plume interaction with supersonic freestream and key recirculation zones for conical deflector with separation distances of (a) $(1/16)D$, (b) $(1/8)D$, (c) $(1/4)D$ and (d) $(1/2)D$ between 1st stage and second stage, where D is the nozzle diameter.

increased.

Figure 4.20 demonstrate variation of aero-thermodynamic coefficients on the top of 1st stage along the arc length and comparison between various separation distances. The C_h plot shows the same trend as mentioned in the previous sections. The value of C_h decreases as we move away from nose center of 1st stage. However, the gradient of temperature increases as separation distance is reduced which can be seen by steep slopes in case of $(1/16)D$ and gradual slopes in case of $(1/2)D$. In the C_p plot, stronger and weak shock wave can be observed between arc length 0 m to 0.1 m, for $(1/8)D$ and $(1/16)D$ separation distance, respectively. For $(1/16)D$ weak shock is also observed at arc length = 0.64 m. However, for $(1/4)D$ and $(1/2)D$ no shock waves are observed. From Fig. 4.20 (c), it can be concluded that the normalised shear stress increases with reducing separation distance. Also, the steep slope observed in $(1/16)D$ case diminishes as the separation distance is increased.

Figure 4.21 show case the variation of aero-thermodynamic coefficients on the outer nozzle wall and comparison between various separation distances. C_h for all separation distances increases with increase in arc length with a sudden rise near the nozzle exit. This sudden rise is due to the enhanced heat transfer because of the recirculation zone found near the nozzle exit. With the increasing separation distance the backflow of plumes should usually reduce. However, astonishing results are found when the separation distance is $(1/2)D$. For $(1/16)D$ and $(1/8)D$, the plumes difuses into the freestream upstream to nozzle

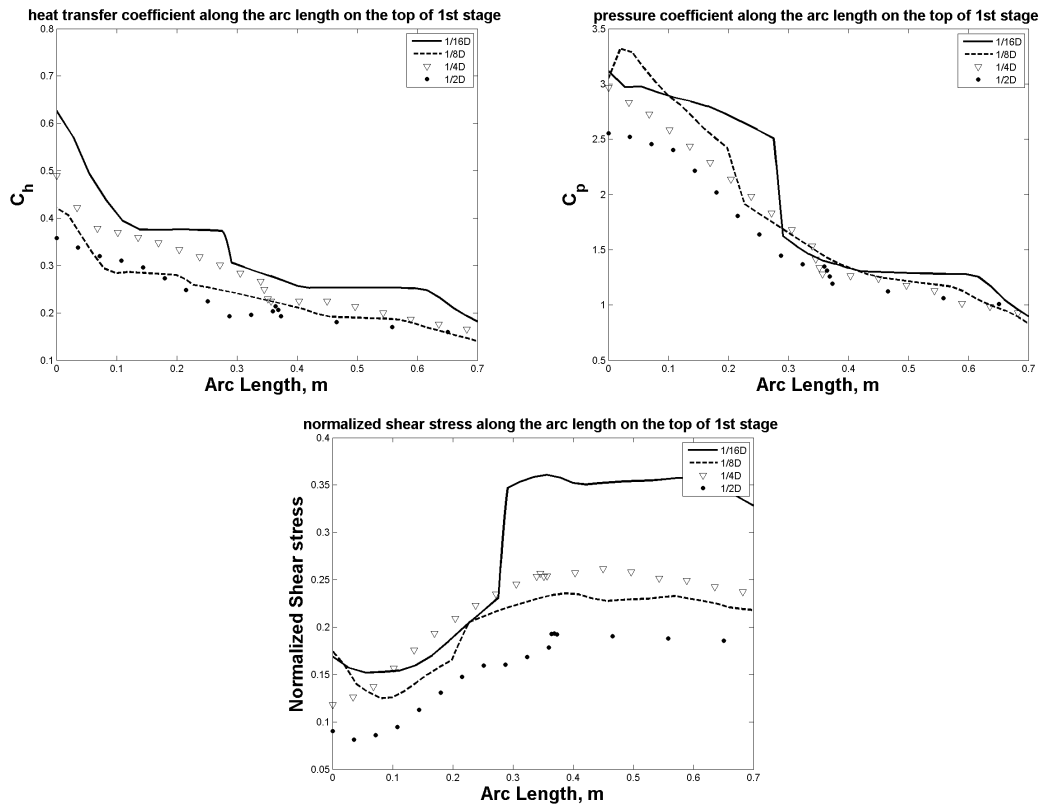


Figure 4.20: Variation of aero-thermodynamic coefficients on the top of 1st stage along the arc length and comparison between various separation distances. Here, (a) heat transfer coefficient (C_h), (b) pressure coefficient (C_p) and (c) normalized shear stress.

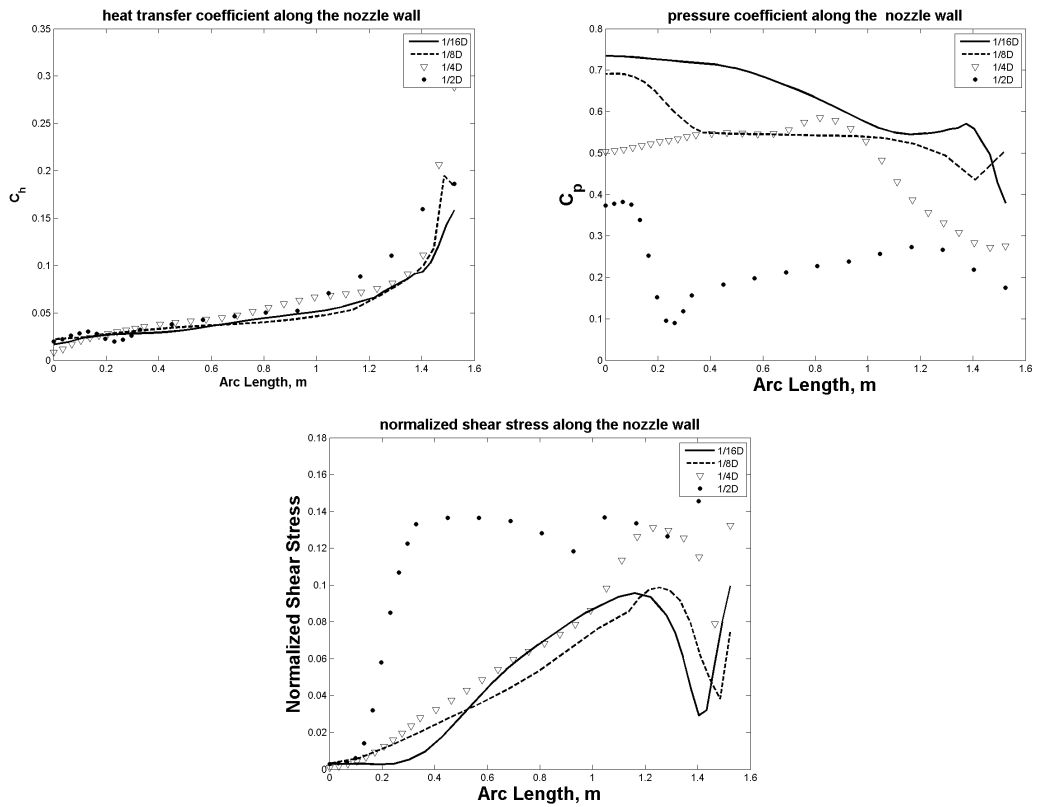


Figure 4.21: Variation of aero-thermodynamic coefficients on the outer nozzle wall and comparison between various separation distances. Here, (a) heat transfer coefficient (C_h), (b) pressure coefficient (C_p) and (c) normalized shear stress.

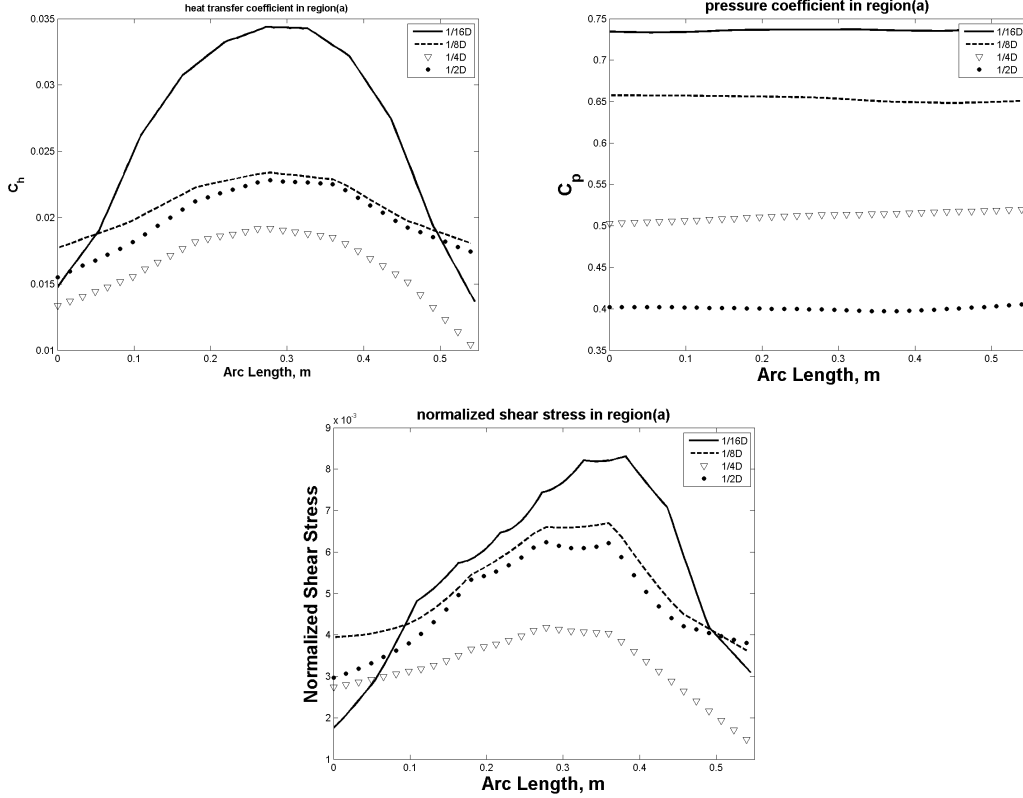


Figure 4.22: Variation of aero-thermodynamic coefficients on the interior of aftwall along the arc length and comparison between various separation distances. Here, (a) heat transfer coefficient (C_h), (b) pressure coefficient (C_p) and (c) normalized shear stress.

exit while, for (1/2)D, the plumes diffuses into the downstream to the nozzle wall. Hence, maximum plume flow in the cavity is observed for (1/16)D and minimum is observed for (1/2)D. Flow separation as discussed in previous section is higher for (1/4)D as compared to (1/2)D which results in higher temperature at the nozzle wall for (1/2)D. This is also supported by the steep slope of (1/4)D near the nozzle exit wall location. Steep slope in (1/8)D can be attributed to the shock formation. Due to high velocity plumes in (1/16)D, flow separates much before the nozzle exit which is indicated by lowest temperature at nozzle exit wall location i.e. 1.5 m. C_p plot shows that for (1/16)D, there is continuous expansion till arc length = 1.2 m. After that, shock wave is formed and then again expansion. Similar kind of trend is observed for (1/8)D. Shock is formed at arc length = 1.4 m. For (1/2)D case, shock is formed at 0.2 m arc length. Hence, as the separation distance is increased the shock wave first moves toward the exit until (1/8)D and as the separation distance is further increased it starts moving towards the throat.

Figure 4.22 shows the variation of aero-thermodynamic coefficients on the interior of aftwall along the arc length and comparison between various separation distances. Heat transfer in region 'a' decreases with increase in separation distance until (1/4)D. After that

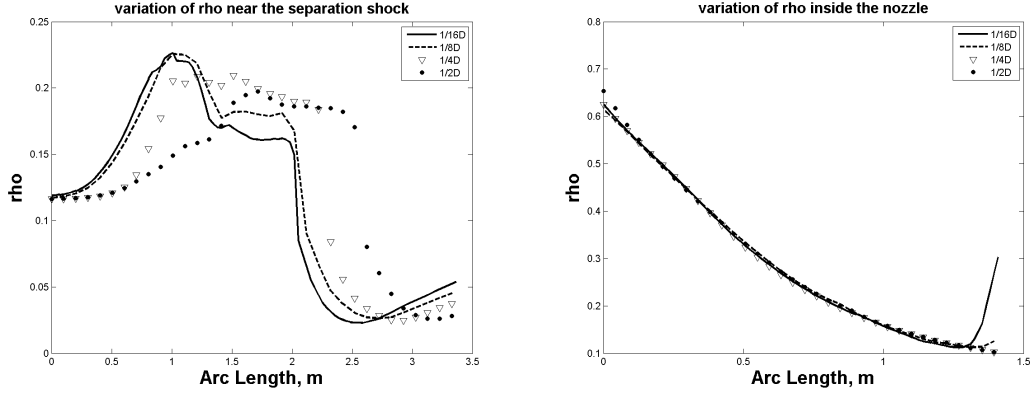


Figure 4.23: (a) The density variation on the outersurface of aftwall.(b) The centerline density variation inside the nozzle starting from throat to the exit. Comparisons are made between various separation distances for a conical plume deflector.

distance, it start increasing which can be seen by a higher C_h of (1/2)D as compared to (1/4)D (see Fig (a)). Since the plume flow is maximum in (1/16)D, therefore due to the reattachment maximum heat transfer can be observed, that takes place in region 'a' for (1/16)D configuration at arc length of 0.3 m. The reduced separation can be seen by high value of C_h for (1/2)D in comparison to (1/4)D. From Fig. (b) C_p in region 'a' remains almost constant for all configurations. C_p decreases with increase in separation distance. At the point joining nozzle wall and region 'a', normalised shear stress is minimum for (1/16)D and maximum for (1/8)D. As the separation distance is increased the maximum normalised shear stress decreases until 54° , then it again start increasing with increase in cone angle.

Figure 4.23 (a) shows the density variation on the outersurface of aftwall. The steep slopes for (1/16)D and (1/8)D indicates formation of strongest shock waves. As the separation distance is increased, the slopes become gradual. This shows that the strength of separation is decreased with increasing separation distance. Fig. 4.23 (b) shows the centerline density variation inside the nozzle starting from throat to the exit. The gradual decrease in pressure shows the expansion and acceleration of the plume. However, a strong impingement shock can be observed for (1/16)D while a weaker one can be seen for (1/8)D. As the separation distance is increased the shock moves toward the exit of nozzle.

Deflector type	Top of 1 st stage	Outer nozzle wall	Region 'a'
conical	0.299	0.0591	0.027
Spherical	0.218	0.0586	0.0237
blunt	0.281	0.0628	0.0495

Table 4.2: Heat transfer coefficient on the top of 1st stage, outer nozzle wall and region 'a' for conical, spherical and blunt configurations, respectively.

Cone angle	Top of 1 st stage	Outer nozzle wall	Region 'a'
22 ⁰	0.22	0.0686	0.021
33 ⁰	0.207	0.0723	0.0211
54 ⁰	0.299	0.0591	0.027
60 ⁰	0.279	0.062	0.0264

Table 4.3: Heat transfer coefficient on the top of 1st stage, outer nozzle wall and region 'a' for conical configuration with varying cone angles of 22⁰, 33⁰, 54⁰ and 60⁰.

Separation distance	Top of 1 st stage	Outer nozzle wall	Region 'a'
(1/16)D	0.299	0.0591	0.027
(1/8)D	0.233	0.0686	0.0209
(1/4)D	0.255	0.0606	0.0163
(1/2)D	0.215	0.0534	0.02

Table 4.4: Heat transfer coefficient on the top of 1st stage, outer nozzle wall and region 'a' for conical configuration with varying separation distance of (a) (1/16)D, (b) (1/8)D, (c) (1/4)D and (d) (1/2)D.

Chapter 5

Conclusions and future work

Among conical, spherical and blunt configuration, heating effect on aft skirt and nozzle wall is minimum for spherical but high normalised shear stress can lead to uneven turning moments. By increasing the sharpness of spherical configuration, the normalised shear stress can be optimized.

33° cone angle is best from the heating prospective in region 'a' and top of 1st stage. However, significant heating can be observed on the nozzle wall. For 54° configuration heating on nozzle wall is minimum. Hence, studies for cone angles between 33° and 54° can be conducted to find an optimized cone angle.

With the increasing separation distance, the overheating can be reduced. However, with the increasing distance the length of the launcher vehicle also increases and the adapter holding the 1st and 2nd stage also becomes longer. This may lead to aerodynamic instability. Hence optimization need to be done.

Following points are listed down which can be used for future work.

1. We are using spalart-Allamaras one equation turbulence model. Various turbulence models can be implemented and the results can be compared.
2. Configurations with conical deflector with cone angles between 33° and 54° can be studied to find the best optimized cone angle.
3. Various plume deflectors like bi-cone, elliptical, parabolic etc. can be studied.

References

- [1] C. Yoon, Y. Matsutomi, W. E. Anderson, and C. L. Merkle. Investigation of the Cap-Shock Pattern in a Thrust-Optimized Rocket Nozzle .
- [2] A. D. I. J. T. d. C. J.B. Fulindi, L.E.L.D. Costa and J. Ettl. THE VLM-1 Launch system concept,in:Proceedings of the 63rd International Astronautical Congress. 2012 .
- [3] D. Schwamborn. Development of the TAU-code for aerospace applications, in:.. *Proceedings of the 50th NAL International Conference on Aerospace Science and Technology* .
- [4] A. G. D. Schwamborn and R. Heinrich. The DLR TAU-code: recent applications in research and industry. *Proceedings of the European Conference on Computational Fluid Dynamics, TU Delft, Netherlands* .
- [5] P. Huseman. CFD analysis of Titan IV fire-in-the-hole staging, in: Proceedings of the 33rd Aerospace Sciences Meeting and Exhibit. 1995 .
- [6] Y. I. T. Nakajima and H. Matsuo. study of fire-in-the-hole system for M-V launch vehicle. 1991 .
- [7] NASA. NASA space vehicle design criteria: flight separation mechanisms. *SP-8056* .
- [8] G. Dettleff. Plume flow and plume impingement in space technology. *Progress in Aerospace Sciences* 28, (1991) 1–71.
- [9] C. Zahringert and G. Sachs. Wind tunnel tests for separation dynamics modeling of a two-stage hypersonic vehicle .
- [10] D. E. Reubush. X-43A Stage Separation System–A Flight Data Evaluation .
- [11] K. J. Murphy and W. I. Scallion. Experimental stage separation tool development in NASA Langleys Aerothermodynamics Laboratory. *AIAA Paper* 6127.
- [12] P. G. Buning, T.-C. Wong, A. D. Dilley, and J. L. Pao. Prediction of hyper-x stage separation aerodynamics using CFD .

- [13] P. Liever, S. Habchi, W. Engelund, and J. Martin. Stage separation analysis of the X-43A research vehicle. In 22nd applied aerodynamics conference and exhibit (AIAA paper 2004-4725), Providence, Rhode Island. 2004 .
- [14] M. Mirzaei, B. Najafie Nia, and A. Shadaram. Numerical simulation of stage separation manoeuvre with jet interaction. *Aircraft Engineering and Aerospace Technology* 78, (2006) 217–225.
- [15] A. Pizzicaroli, F. Paglia, E. Lambiase, C. Contini, C. Dumaz, and F. Stella. Vega Launcher Aerodynamics at Separation of First Stage. In 43rd AIAA/ASME/SAE/ASEE Joint Propulsion Conference & Exhibit .
- [16] S. Zhang and X. Zhao. Computational studies of stage separation with an unstructured chimera grid method. *AIAA Paper-2007-5409* .
- [17] B. Pamadi, J. Pei, J. T. Pinier, S. D. Holland, P. F. Covell, and G. H. Klopfer. Aerodynamic Analyses and Database Development for Ares I Vehicle First-Stage Separation. *Journal of Spacecraft and Rockets* 49, (2012) 864–874.
- [18] G. H. Klopfer, J. E. Kless, H. C. Lee, J. T. Onufer, S. Pandya, and W. M. Chan. Validation of Overflow for Computing Plume Effects during the Ares I Stage Separation Process. *AIAA Paper* 170, (2011) 2011.
- [19] Y. Wang, H. Ozawa, H. Koyama, and Y. Nakamura. Simulation of supersonic stage separation of capsule-shaped abort system by aerodynamic interaction. In 20th AIAA computational fluid dynamics conference (AIAA paper 2011-3064), Honolulu, Hawaii. 2011 .
- [20] Y. Li, B. Reimann, and T. Eggers. Numerical investigations on the aerodynamics of SHEFEX-III launcher. *Acta Astronautica* 97, (2014) 99–108.
- [21] A. Kurganov and E. Tadmor. New High-Resolution Central Schemes for Nonlinear Conservation Laws and Convection-Diffusion Equations. *J. Comput. Phys* 160, (2000) 241–282.
- [22] A. Wulf and V. Akdag. Tuned grid generation with ICEM CFD .
- [23] H. G. Weller, G. Tabor, H. Jasak, and C. Fureby. A tensorial approach to computational continuum mechanics using object-oriented techniques. *Computers in physics* 12, (1998) 620–631.
- [24] H. Jasak. OpenFOAM: a year in review. In 5th OPENFOAM Workshop, Gothenburg, Sweden, June. 2010 21–24.

- [25] E. Casartelli and L. Mangani. Object-Oriented Open-Source CFD for Turbomachinery Applications: A Review and Recent Advances. In ASME Turbo Expo 2013: Turbine Technical Conference and Exposition. American Society of Mechanical Engineers, 2013 V06BT37A036–V06BT37A036.
- [26] A. Kurganov and E. Tadmor. New high-resolution central schemes for nonlinear conservation laws and convection–diffusion equations. *Journal of Computational Physics* 160, (2000) 241–282.
- [27] A. Kurganov, S. Noelle, and G. Petrova. Semidiscrete central-upwind schemes for hyperbolic conservation laws and Hamilton–Jacobi equations. *SIAM Journal on Scientific Computing* 23, (2001) 707–740.
- [28] C. J. Greenshields, H. G. Weller, L. Gasparini, and J. M. Reese. Implementation of semi-discrete, non-staggered central schemes in a colocated, polyhedral, finite volume framework, for high-speed viscous flows. *International journal for numerical methods in fluids* 63, (2010) 1–21.
- [29] H. S. F. S. U. OPENFOAM. Mecánica Computacional, Volume XXXI. Number 16. Aerospaciale Technology (A) .
- [30] S. Nakao, M. Kashitani, T. Miyaguni, and Y. Yamaguchi. A study on high subsonic airfoil flows in relatively high Reynolds number by using OpenFOAM. *Journal of Thermal Science* 23, (2014) 133–137.
- [31] H. K. Versteeg and W. Malalasekera. An introduction to computational fluid dynamics: the finite volume method. Pearson Education, 2007.
- [32] OpenFOAM.
- [33] J. Longo. Shefex-a Low Cost Highly Efficient Flight Experiment. In Fifth European Symposium on Aerothermodynamics for Space Vehicles, volume 563. 2005 425.
- [34] T. Eggers, J. Longo, M. Hoerschgen, and A. Stamminger. The hypersonic flight experiment SHEFEX. *AIAA Paper* 3294, (2005) 2005.
- [35] S. Lawson and G. Barakos. Review of numerical simulations for high-speed, turbulent cavity flows. *Progress in Aerospace Sciences* 47, (2011) 186–216.
- [36] J.-C. LENGRAND, J. ALLERGE, and M. Raffin. Heat transfer to a surface impinged upon by a simulated underexpanded rocket exhaust plume. *Rarefied gas dynamics* 980–993.